

Chemistry in disks

XI. Sulfur-bearing species as tracers of protoplanetary disk physics and chemistry: the DM Tau case

D. Semenov^{1,2}, C. Favre³, D. Fedele³, S. Guilloteau^{4,5}, R. Teague⁶, Th. Henning¹,
A. Dutrey^{4,5}, E. Chapillon⁷, F. Hersant^{4,5}, and V. Piétu⁷

¹ Max-Planck-Institut für Astronomie, Königstuhl 17, 69117 Heidelberg, Germany
e-mail: semenov@mpia.de

² Department of Chemistry, Ludwig Maximilian University, Butenandtstraße 5–13, 81377 Munich, Germany

³ INAF, Osservatorio Astrofisico di Arcetri, Largo Enrico Fermi 5, 50125 Firenze, Italy

⁴ LAB, Université de Bordeaux, B18N, Allée Geoffroy, Saint-Hilaire, 50023, 33615 Pessac Cedex, France

⁵ CNRS, Université de Bordeaux, B18N, Allée Geoffroy, Saint-Hilaire, 50023, 33615 Pessac Cedex, France

⁶ Department of Astronomy, University of Michigan, 1085 S. University Avenue, Ann Arbor, MI 48109, USA

⁷ IRAM, 300 Rue de la Piscine, 38046 Saint-Martin-d'Hères, France

Received 7 March 2018 / Accepted 19 June 2018

ABSTRACT

Context. Several sulfur-bearing molecules are observed in the interstellar medium and in comets, in strong contrast to protoplanetary disks where only CS, H₂CS, and SO have been detected so far.

Aims. We combine observations and chemical models to constrain the sulfur abundances and their sensitivity to physical and chemical conditions in the DM Tau protoplanetary disk.

Methods. We obtained 0.5'' Atacama Large Millimeter Array observations of DM Tau in Bands 4 and 6 in lines of CS, SO, SO₂, OCS, CCS, H₂CS, and H₂S, achieving a ~5 mJy sensitivity. Using the non-Local Thermodynamical Equilibrium radiative transfer code RADEX and the forward-modeling tool DiskFit, disk-averaged CS column densities and upper limits for the other species were derived.

Results. Only CS was detected with a derived column density of ~2–6 × 10¹² cm⁻². We report a first tentative detection of SO₂ in DM Tau. The upper limits range between ~10¹¹ and 10¹⁴ cm⁻² for the other S-bearing species. The best-fit chemical model matching these values requires a gas-phase C/O ratio of ≥1 at $r \gtrsim 50$ –100 au. With chemical modeling we demonstrate that sulfur-bearing species could be robust tracers of the gas-phase C/O ratio, surface reaction rates, grain size and UV intensities.

Conclusions. The lack of detections of a variety of sulfur-bearing molecules in DM Tau other than CS implies a dearth of reactive sulfur in the gas phase, either through efficient freeze-out or because most of the elemental sulfur is in other large species, as found in comets. The inferred high CS/SO and CS/SO₂ ratios require a non-solar C/O gas-phase ratio of ≥1, consistent with the recent observations of hydrocarbon rings in DM Tau. The stronger depletion of oxygen-bearing S-species compared to CS is likely linked to the low observed abundances of gaseous water in DM Tau and points to a removal mechanism of oxygen from the gas.

Key words. astrochemistry – protoplanetary disks – radio lines: planetary systems – radio lines: stars – circumstellar matter

1. Introduction

One of the most exciting topics in astronomy is to understand the physical and chemical link between various stages of the star and planet formation processes and the properties of planetary systems and exoplanet atmospheres (e.g., [Mordasini et al. 2012](#); [Mollière et al. 2015](#); [Cridland et al. 2017](#)). Infrared and (sub-)millimeter observations of the dust continuum and molecular lines are used to study these environments. The compact, ≤100–1000 au sizes and the low, ≤0.01–0.1 M_{\odot} gas masses make such studies particularly challenging for protoplanetary disks, even with the most powerful observational facilities like Atacama Large Millimeter Array (ALMA), Northern Extended Millimeter Array (NOEMA), and the Extended Very Large Array (EVLA). Thus, compared to more than 200 molecules discovered in the interstellar medium (ISM)¹, only ~20 species and

their isotopologues were detected in disks (see e.g., [Henning & Semenov 2013](#); [Dutrey et al. 2014](#); [Bergin et al. 2015](#)).

Using this limited set of molecular tracers, crucial information about disk physics, chemistry, and kinematics at outer radii of ≥50–100 au has been obtained. From the relatively easy-to-detect CO isotopologues disk orientations, sizes, temperature structures, and indirect disk gas masses have been derived (e.g., [Williams & Best 2014](#); [Ansdell et al. 2016, 2017](#); [Guilloteau et al. 2016](#); [Pascucci et al. 2016](#); [Schwarz et al. 2016](#); [Long et al. 2017](#)). More reliable gas mass measurements using HD have been obtained with *Herschel* for TW Hya, DM Tau, and GM Aur ([Bergin et al. 2013](#); [McClure et al. 2016](#); [Trapman et al. 2017](#)). The importance of CO-regulated ice chemistry for the synthesis of complex organic molecules has been supported by the H₂CO observations of DM Tau ([Loomis et al. 2015](#)) and CH₃OH observations of TW Hya ([Walsh et al. 2016](#); [Parfenov et al. 2017](#)).

One of the most intriguing ALMA results is evidence of substantial depletion of elemental C and O in T Tauri disks,

¹ <http://www.astro.uni-koeln.de/cdms/molecules>

with C/O becoming >1 in a molecular layer (Bergin et al. 2016; Öberg & Bergin 2016). Schwarz et al. (2016) and Kama et al. (2016) have found that CO is depleted by two orders of magnitude in the TW Hya disk, which cannot be solely explained by the CO freeze-out in the midplane, while the CO depletion in the warmer Herbig Ae disk HD 100546 is negligible (Kama et al. 2016). Similarly, McClure et al. (2016) derived CO depletion of up to a factor of five for DM Tau and up to a factor of ~ 100 for GM Aur. Plausible mechanisms for this depletion are: 1) warm surface chemistry that converts volatile CO to less volatile CO_2 , 2) He^+ destruction of CO, which liberates carbon that is converted into refractory complex organics, or 3) preferential removal of oxygen from the disk molecular layer by the freeze-out of water onto sedimenting large dust grains (e.g., Semenov & Wiebe 2011; Favre et al. 2013; Krijt et al. 2016; Öberg & Bergin 2016; Rab et al. 2017a). The higher freeze-out temperature of water, $T_{\text{fr}} \sim 140\text{--}160$ K, favors its depletion over the volatile CO ($T_{\text{fr}} \sim 20\text{--}25$ K) and N_2 ($T_{\text{fr}} \leq 16\text{--}18$ K) (Mumma & Charnley 2011; Qi et al. 2013; Du et al. 2015; Öberg & Bergin 2016; Krijt et al. 2016).

Despite these promising results, almost nothing is known about the sulfur content in disks. So far, only CS has been detected in dozens of disks and SO has only been detected in several younger, actively accreting disks including the disk of the Herbig A0 star AB Aur and Class I sources (Dutrey et al. 2011; Guilloteau et al. 2016; Pacheco-Vázquez et al. 2016; Sakai et al. 2016). Dutrey et al. (2011) could not detect the SO and H_2S lines with the IRAM 30-m in LkCa15, DM Tau, GO Tau, and MWC 480. They performed a careful analysis of the previously observed CS lines and the upper limits of the SO column densities and concluded that the best-fit model requires a C/O ratio of 1.2, yet this model failed to reproduce the H_2S upper limits by at least one order of magnitude. The CS emission in TW Hya reveals a complex radial distribution with a surface density gap at around 95 au and low turbulent velocities (Teague et al. 2016, 2017). Using the IRAM 30-m antenna, Chapillon et al. (2012a) observed CCS in DM Tau and MWC 480 and obtained upper limits on the CCS column densities in these disks, $\lesssim 1.5 \times 10^{12} \text{ cm}^{-2}$. Recently, H_2CS was found in the Herbig Ae disk of MWC 480 by Loomis et al. (2017; priv. comm.), where CS was also detected. Finally, Booth et al. (2018) have recently detected SO emission in HD 100546 that does not come solely from the Keplerian disk, but shows an additional non-disk component (a disk wind, a warp, or shocked gas).

This is in contrast to the studies of the ISM, where sulfur-bearing species are commonly observed and used as tracers of chemical ages (e.g., CCS/NH_3 ; Suzuki et al. 1992), temperature/shocks (SO, SO_2 , OCS; Esplugues et al. 2014), X-ray irradiation (SO; Stäuber et al. 2005), grain processing (SO/ H_2S , SO/ SO_2 ; Charnley 1997), and turbulent transport (CCS/CO; Semenov & Wiebe 2011). The S-bearing molecules such as H_2S , SO, SO_2 , CS, CS_2 , H_2CS , S polymers, and other complex S-bearing chains and organics were detected in comets and satellites of Jovian planets in our solar system (e.g., Boissier et al. 2007; Le Roy et al. 2015; Calmonte et al. 2016). Recently, sulfur-bearing species have been detected in the molecular disk around the late-type Sun-like AGB star (Kervella et al. 2016).

The sulfur-bearing amino acids cysteine and methionine, as well as OCS acting as a catalyst in peptide synthesis, play an important role in biochemistry and hence sulfur chemistry could be related to the origin of life (Brosnan & Brosnan 2006; Chen et al. 2015). In order to make progress in our understanding of

the importance of the delivery of S-bearing molecules to early Earth and Earth-like planets, a better understanding of the sulfur content of protoplanetary disks is required. Intriguingly, modern astrochemical models cannot fully reproduce the observed abundances or upper limits of sulfur-bearing species. The main reasons are likely uncertainties in the reaction rates, missing key formation routes, or unaccounted major reservoirs of sulfur (see e.g., Druard & Wakelam 2012; Loison et al. 2012; Vidal et al. 2017).

The main goals of this paper are twofold. First, we aim to study in detail sulfur chemistry in the DM Tau disk using ALMA observations that are several times more sensitive than the previous observations. Second, we aim to investigate the sensitivity of the disk sulfur chemistry to various physical and chemical parameters, using an appropriate DM Tau physical-chemical model. The paper is organized as follows. In Sect. 2 our ALMA Cycle 3 observations are presented. Disk-averaged column densities and upper limits are derived in Sect. 3. In Sects. 4.1 and 4.2 the adopted physical and chemical models of the DM Tau disk are described, and the parameter space to be calculated is presented. The comparison between the observed values and the grid of DM Tau models is discussed in Sect. 5. Discussion and conclusions follow.

2. Observations

2.1. ALMA observations and data reduction

Observations of DM Tau were carried out with ALMA on June 22 (in Band 6) and July 26, 2016 (in Band 4) as part of the ALMA project 2015.1.00296.S, PI: Dmitry Semenov. The phase tracking center was $\alpha_{J2000} = 04^{\text{h}}33^{\text{m}}48^{\text{s}}.747$, $\delta_{J2000} = 18^{\circ}10'09''.585$. The systemic velocity of the source was set to $v_{\text{LSR}} = 6 \text{ km s}^{-1}$. More specifically, Band 4 data were taken with 45 antennas and baselines from 15.1 m up to 1.1 km with an on-source time of about 2 min. The Band 4 spectral setup consisted of six spectral windows with 480 channels each with a channel width of 122.07 kHz ($\sim 0.3 \text{ km s}^{-1}$), covering about 0.4 GHz between 145.926 and 159.010 GHz, and one continuum spectral window with the 2 GHz bandwidth (128×15.625 MHz channels) centered at 145.021 GHz. The quasars J0510+1800 and J0431+2037 were used as bandpass, flux, and phase calibrators. The Band 6 data were taken with 37 antennas and baselines from 15.1 up to 704.1 m with an on-source time of about 20 min, using J0510+1800 and J0423–0120 as bandpass, flux, and phase calibrators. The Band 6 spectral setup consisted of three spectral windows with 240 channels each with a channel width of 244.141 kHz ($\sim 0.3 \text{ km s}^{-1}$), covering about 0.2 GHz between 215.195 and 218.936 GHz, and one continuum spectral window with the 2 GHz bandwidth (128×15.625 MHz channels) centered at 232.012 GHz.

Data reduction and continuum subtraction in the uv -space were performed through the Common Astronomy Software Applications (CASA) software (McMullin et al. 2007), version 4.5.3. The continuum image at 145.021 GHz was self-calibrated, and the solutions were applied to the lines observed in Band 4 in order to improve the signal-to-noise ratio (S/N), in particular for the SO_2 transitions. To further optimize the sensitivity, data from Bands 4 and 6 were cleaned using the “natural” weighting. The resulting synthesized beam size is $0.61'' \times 0.58''$ at a positional angle of $\sim 28^\circ$ for the 145 GHz continuum image, with the 1σ rms of $7.6 \times 10^{-5} \text{ Jy beam}^{-1}$. For the line images at Bands 4 and 6 the synthesized beams are similar,

Table 1. Spectroscopic line parameters.

Line	Frequency (GHz)	E_u (K)	$S\mu^2$ (D^2)
CS 3 – 2	146.96903	14	11
CCS $N = 12 - 11, J = 13 - 12$	156.98165	51	108
H ₂ S 2 _{2,0} – 2 _{1,1}	216.71044	84	2
OCS 12 – 11	145.94681	46	9
OCS 18 – 17	218.90336	100	9
SO $^3\Sigma v = 0, 3_4 - 2_3$	158.97181	29	6
SO $^3\Sigma v = 0, 5_5 - 4_4$	215.22065	44	11
SO ₂ $v = 0, 4_{2,2} - 4_{1,3}$	146.60552	19	6
SO ₂ $v = 0, 3_{2,2} - 3_{1,3}$	158.19974	15	4

Notes. Column 3: upper state energies. Column 4: line strengths. The data are taken from the CDMS database (Müller et al. 2005), <https://www.astro.uni-koeln.de/cdms/catalog>.

$\approx 0.6'' \times 0.5''$ (positional angle is 23°), with a spectral resolution of $\sim 0.3 \text{ km s}^{-1}$ and a 1σ rms sensitivity of $5 \times 10^{-3} \text{ Jy beam}^{-1}$.

2.2. Line imaging

The targeted molecular lines, their frequencies, and spectroscopic parameters are listed in Table 1. The only detected emission ($>3\sigma$) visible in the continuum-subtracted integrated intensity and spectral maps was CS (3 – 2) (see Figs. 1 and 2). Both maps are relatively noisy because the ALMA Band 4 integration time was short, only about 2 min on-source. The observed line parameters assuming a source size of $4''$, which is estimated from the CS integrated emission map over the line profile, are presented in Table 2.

To increase the signal, we applied the pixel deprojection and azimuthal averaging technique as presented in Teague et al. (2016), Yen et al. (2016), and Matrà et al. (2017). For deprojection we used an inclination angle of -34° , a positional angle of 27° , a distance of 140 pc, and a stellar mass of $0.55 M_\odot$ (Teague et al. 2015; Simon et al. 2017). After such deprojection, a double-peaked spectrum typical for Keplerian disks becomes a single-peaked spectrum with a narrower line width. The resulting shifted spectra are presented in Fig. 3 for Band 4 and in Fig. 4 for Band 6, respectively. As can be clearly seen, the only firmly detected line in our dataset is CS (3 – 2), with a peak $S/N \geq 14$. There is a tentative detection of the SO₂ ($3_{2,2} - 3_{1,3}$) line, with a peak $S/N \approx 4.7$, albeit the signal is slightly shifted from the velocity center by $+1 \text{ km s}^{-1}$ (Fig. 3, left bottom panel). The rest of the lines are not detected.

3. Observed CS column density and the upper limits for SO, SO₂, H₂S, OCS, and CCS

3.1. Fitting with RADEX

Since we are mainly dealing with non-detections, and our CS data are noisy, we decided to start with a simple approach based on Fedele et al. (2012, 2013) to derive disk-averaged vertical column densities or their upper limits. The ALMA data in the CASA format were exported as FITS files and analyzed in GILDAS software². Each individual integrated spectrum was fitted with a Gaussian function, assuming a source diameter of $4''$

² <https://www.iram.fr/IRAMFR/GILDAS/>

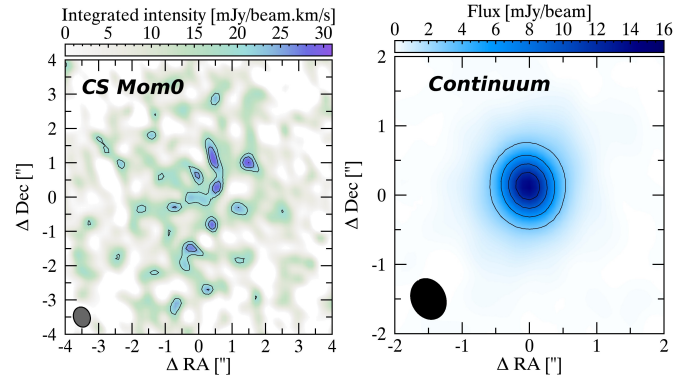


Fig. 1. Left panel: ALMA Band 4 CS (3 – 2) 0th-moment map of the DM Tau disk. Right panel: dust continuum map of the DM Tau disk at 146.969 GHz. The first contours and the level steps are at 3σ rms.

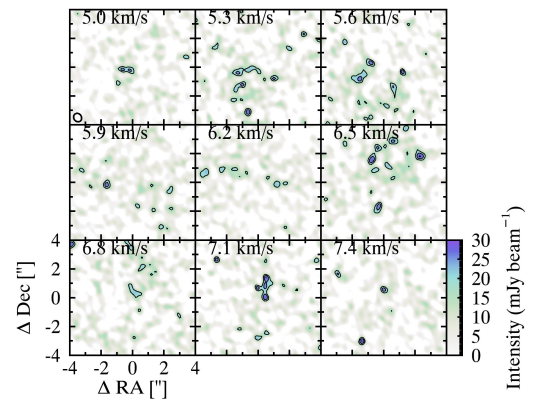


Fig. 2. ALMA Band 4 spectral map showing CS (3 – 2) in the DM Tau disk. The channel spacing is 0.3 km s^{-1} . The first contour and the level step are at 3σ rms.

(560 au at a distance of 140 pc), based on the CS 0th-moment map (see Table 2). To convert line fluxes to column densities, we employed a widely used RADEX code³ (van der Tak et al. 2007). The code uses a uniform physical structure to perform line radiative transfer with the Large Velocity Gradient (LVG) method based on statistical equilibrium calculations with collisional and radiative processes and background radiation. Optical depth effects are accounted for with an escape probability method. The molecular data were taken from the Leiden Atomic and Molecular Database (LAMDA⁴; see Schöier et al. 2005). A local line width of 0.14 km s^{-1} was assumed for all molecules based on the previous CS observations by Guilloteau et al. (2012). When two transitions were observed, they were both stacked and taken into account.

By varying excitation temperature, volume density, and column density, the χ^2 values between the observed and modeled CS line fluxes were computed and minimized. The upper limits of the column densities of the other non-detected sulfur-bearing species were derived in a similar manner, using the observed 3σ rms as the line flux limit. We were not able to analyze the CCS data as there are no collisional rate data in the LAMDA and Basecol⁵ databases. The resulting χ^2 distributions for the assumed volume densities of 10^6 , 10^7 , and 10^8 cm^{-3} representative of the outer DM Tau molecular layer are shown in Fig. 5.

³ <http://home.strw.leidenuniv.nl/~moldata/radex.html>

⁴ <http://home.strw.leidenuniv.nl/~moldata/>

⁵ <http://basecol.obspm.fr/>

Table 2. Line parameters for the observed sulfur-bearing transitions towards DM Tau.

Molecule	Transition	v_{LSR}	Δv_{FWHM}	I_{peak}	$\int T dV$
		(km s ⁻¹)	(km s ⁻¹)	(mJy)	(Jy km s ⁻¹)
CS	3 – 2	6.2(0.3)	1.9(0.6)	520(100)	1.1(0.3)
CCS $N = 12 - 11$	13 – 12	≤ 130	...
H ₂ S	2 _{2,0} – 2 _{1,1}	≤ 10	...
OCS $v = 0$	12 – 11	≤ 130	...
OCS $v = 0$	18 – 17	≤ 10	...
SO $^3\Sigma v = 0$	3 ₄ – 2 ₃	≤ 130	...
SO $^3\Sigma v = 0$	5 ₅ – 4 ₄	≤ 10	...
SO ₂ $v = 0$	4 _{2,2} – 4 _{1,3}	≤ 350	...
SO ₂ $v = 0$	3 _{2,2} – 3 _{1,3}	≤ 250	...

Notes. The observed values along with the 3σ uncertainties (given in brackets) obtained by the Gaussian fit. Column 3: LSR velocity. Column 4: full width half maximum line width. Column 5: peak intensity. Column 6: line area.

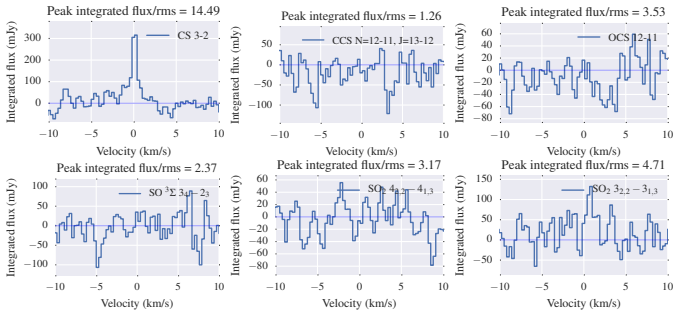


Fig. 3. Pixel deprojected and azimuthally averaged ALMA Band 4 spectra showing CS (3 – 2), CCS ($N = 12 - 11$, $J = 13 - 12$), OCS (12 – 11), SO ($^3\Sigma v = 0$, 3₄ – 2₃), SO₂ ($v = 0$, 4_{2,2} – 4_{1,3}), and SO₂ ($v = 0$, 3_{2,2} – 3_{1,3}) spectral windows in DM Tau.

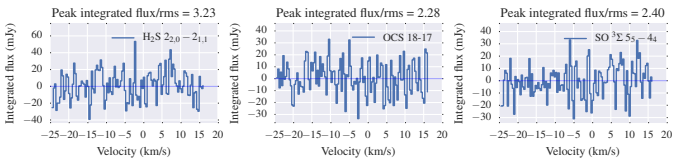


Fig. 4. Pixel deprojected and azimuthally averaged ALMA Band 6 spectra showing H₂S (2_{2,0} – 2_{1,1}), OCS (18 – 17), and SO ($^3\Sigma v = 0$, 5₅ – 4₄) spectral windows in DM Tau.

The computed χ^2 distributions do not depend on the assumed gas density since we have chosen the most easily excited and strong transitions for our observations. The only exception is H₂S (2_{2,0} – 2_{1,1}), which is slightly better fitted with the high-volume density of 10^8 cm⁻³. Due to their low upper state energies $E_u < 20$ K (Table 1), the temperature dependence of the CS and SO₂ fits is rather flat, with the best-fit values of $T_{\text{ex}} \lesssim 100$ K. The higher upper state energies of the H₂S (2_{2,0} – 2_{1,1}), OCS (18 – 17), and SO ($^3\Sigma v = 0$, 5₅ – 4₄) transitions are 84, 100, and 44 K, respectively, which makes them sensitive to the temperature and leads to a prominent temperature dependence of their χ^2 distributions (Fig. 5). The best-fit temperatures and column densities (or their upper limits) are summarized in Table 3.

3.2. Parametric fitting with DiskFit

As the next step, we performed a more elaborate analysis of the data using our DiskFit parametric method (see Piétu et al.

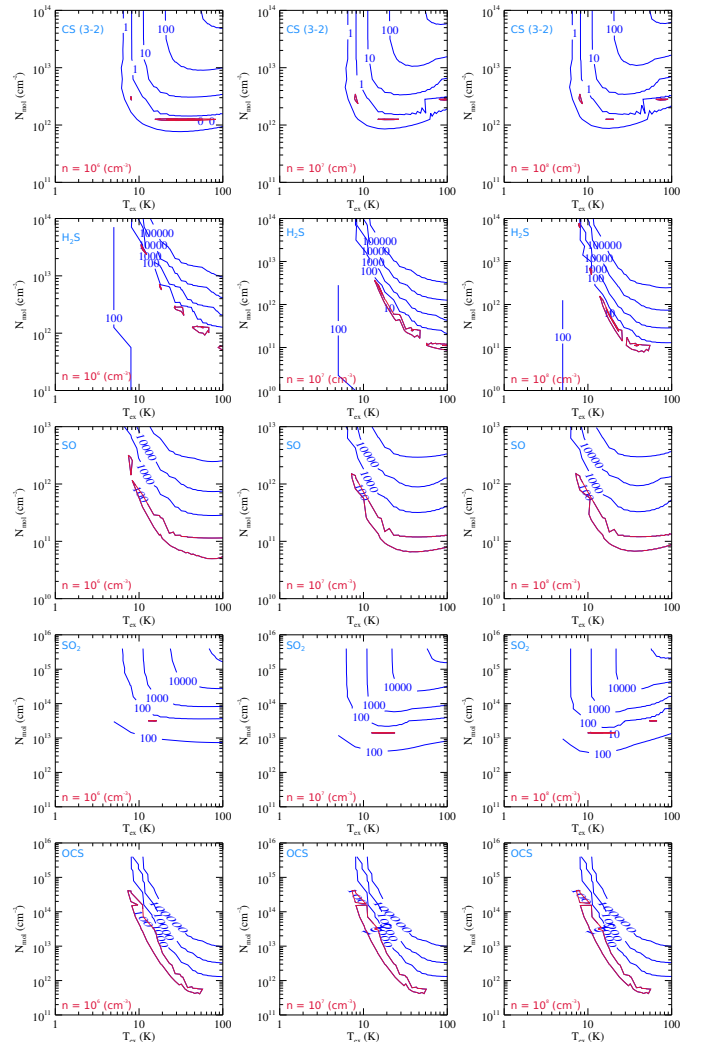


Fig. 5. Computed χ^2 distributions with RADEX code for three volume densities of 10^6 , 10^7 , and 10^8 cm⁻³ and varied T_{ex} and molecular column densities N . *Top to bottom*: results for CS, H₂S, SO, SO₂, and OCS are depicted. The red contours indicate the χ^2 -minima.

2007; Dutrey et al. 2011; Teague et al. 2015). The disk structure is parameterized by radial power laws for the surface density, temperature, kinematics, and molecular column density, which

Table 3. Best-fit temperatures and column densities or 3σ upper limits obtained with RADEX and DiskFit.

Molecule	RADEX		DiskFit, representative radius $r = 300$ au			
	T_{ex} (K)	$N(X)$ (cm^{-2})	T_{ex} (K)	Exponent q	$N(X)$ (cm^{-2})	Exponent p
CS	$\lesssim 100$	$1.5\text{--}3 \times 10^{12}$	10 ± 2	0.5 ± 0.2	$6 \pm 3^a \times 10^{12}$	0.7 ± 0.3
H ₂ S	$\lesssim 100$	$\lesssim 10^{11}\text{--}3 \times 10^{13}$	10^b	0.5	$\lesssim 3 \times 10^{13}$	0.7
OCS	$\lesssim 100$	$\lesssim 5 \times 10^{11}\text{--}4 \times 10^{14}$	10	0.5	$\lesssim 8 \times 10^{11}$	0.7
SO	$\lesssim 100$	$\lesssim 7 \times 10^{10}\text{--}3 \times 10^{12}$	10	0.5	$\lesssim 4 \times 10^{12}$	0.7
SO ₂	$\lesssim 100$	$\lesssim 1\text{--}3 \times 10^{13}$	10	0.5	$\lesssim 10^{13}$	0.7
CCS	10	0.5	$\lesssim 10^{14}$	0.7

Notes. ^(a)The CS is detected at a more than 10σ signal level, but the derived column density error reflects the uncertain partition function. ^(b)For the DiskFit analysis of the sulfur-bearing species other than CS, the best-fit CS temperature and the same type of the radial profile were assumed.

are fitted with a combination of χ^2 minimization and Markov chain Monte Carlo (MCMC) of the observed visibilities in the uv -plane. DiskFit first finds the systemic velocity, the geometrical parameters of the disk system (position of the center, inclination and positional angles, radius of emission), and the disk rotation profile. Next, the dust continuum emission is fitted and dust parameters are obtained. Finally, gas surface density, scale height, temperature, micro-turbulent velocity, and column density distribution are derived.

To increase the S/N of the CS spectrum, the ALMA data were merged with our previous CS (3 – 2) IRAM 30-m data (Dutrey et al. 2011). Neglecting the primary beam correction, which is justified for our $\sim 4''$ emission source, the two visibility sets were merged after resampling in velocity to the coarsest spectral resolution. For the analysis in DiskFit, we used both datasets at their native spectral resolution and fitted them assuming the same underlying physical model. While this approach does not provide a better line image, it preserves the full information on the line widths at the highest possible accuracy. To analyze the non-detected lines we used the best-fit temperature and the radial profiles from the merged CS data. Finally, to get more accurate upper limits for the column densities of SO, SO₂, and OCS, we stacked each of their pairs of observed transitions together (see Figs. 3 and 4). The DiskFit results at a representative outer disk radius of 300 au are given in Table 3.

As can be clearly seen, while the CS column densities derived by both methods are comparable, $\sim 2\text{--}6 \times 10^{12} \text{ cm}^{-2}$, the RADEX-based approach cannot constrain CS excitation temperature, as only one transition of CS was observed. The more advanced DiskFit approach is able to recover radial gradients and points to rather cold CS excitation temperatures of ≈ 10 K in the outer DM Tau disk at ~ 300 au. This is consistent with the low, $\sim 7\text{--}15$ K, excitation temperatures for CO, CCH, CN, HCN, and CS estimated by Piétu et al. (2007), Henning et al. (2010), Chapillon et al. (2012b), and Guilloteau et al. (2012). The further differences between the methods are mainly due to a) differences in the underlying modeling assumptions, where RADEX fits the disk-averaged quantities while DiskFit recovers radial gradients, and b) a left-over degeneracy between the inferred temperature and column density, where both “cold; high-column density” and “warm; low-column density” solutions could exist. For further theoretical analysis of these results in Sect. 5, it is essential that both RADEX and DiskFit converge to a similar best-fit column density ratio for CS/SO of $\gtrsim 1\text{--}3$.

4. Modeling

4.1. Disk physical structure

The DM Tau physical disk model is based on a 1+1D steady-state α -model similar to that of D’Alessio et al. (1999), where equal gas and dust temperatures are assumed. This flaring model was extensively used in our previous studies of DM Tau-like disk chemistry (e.g., Henning et al. 2010; Semenov & Wiebe 2011). The assumption of equal dust and gas temperatures is reasonably accurate for the molecular layers of S-bearing species that do not extend very high into the disk atmosphere (see, e.g., Woitke et al. 2009; Akimkin et al. 2013). The disk model has an outer radius of 800 au, an accretion rate of $5 \times 10^{-9} M_{\odot} \text{ yr}^{-1}$, a viscosity parameter $\alpha = 0.01$, and a total gas mass of $0.066 M_{\odot}$ (Dutrey et al. 2007; Henning et al. 2010; Semenov & Wiebe 2011). This value is close to the upper value of the DM Tau disk mass, $4.7 \times 10^{-2} M_{\odot}$, inferred from the HD *Herschel* observations by McClure et al. (2016).

The Shakura–Sunyaev parametrization (Shakura & Sunyaev 1973) of the turbulent viscosity ν was adopted:

$$\nu(r, z) = \alpha c_s(r, z) H(r), \quad (1)$$

where $H(r)$ is the disk pressure scale height, c_s is the sound speed, and $\alpha = 0.01$ is the dimensionless parameter.

To model turbulent transport along with disk chemical evolution, we used the standard description of the diffusivity coefficient,

$$D_{\text{turb}}(r, z) = \nu(r, z) / S c, \quad (2)$$

where $S c$ is the Schmidt number that describes the efficiency of turbulent diffusivity (see e.g., Schräpler & Henning 2004; Semenov & Wiebe 2011). We considered three regimes of mixing, namely, laminar disk with no mixing ($S c = \infty$), “slow” mixing ($S c = 100$), and “fast” mixing ($S c = 1$). Diffusion of ices is treated similarly to the gas-phase molecules. The calculated thermal and density structure of the disk is shown in Fig. 6.

4.2. Disk chemical model

The adopted chemical model is based on the public gas-grain ALCHEMIC code⁶ (see Semenov et al. 2010; Semenov & Wiebe 2011). The chemical network is based on the osu.2007 ratefile

⁶ http://www.mpia.de/homes/semenov/disk_chemistry_OSU08ggs_UV.zip

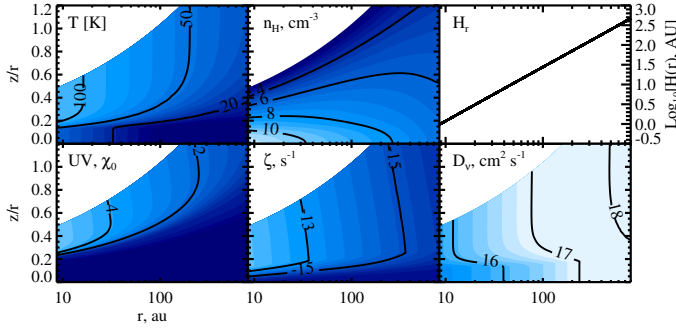


Fig. 6. Adopted DM Tau disk physical structure. *Top row, left to right panels:* spatial distributions of the gas and dust temperature (Kelvin), the gas density (cm^{-3} ; \log_{10} scale), and the pressure scale height (au; \log_{10} scale). *Bottom row, left to right panels:* UV intensity (in χ_0 units of the [Draine 1978](#) interstellar FUV field), the combined ionization rate due to CRPs, stellar X-rays, and short-lived radionuclides (s^{-1}), and the turbulent diffusion coefficient ($\text{cm}^2 \text{s}^{-1}$; \log_{10} scale).

with recent updates to the reaction rates from the Kinetic Database for Astrochemistry (KIDA; [Wakelam et al. 2012](#)).

To calculate ultraviolet (UV) ionization and dissociation rates, the mean far-UV intensity at a given disk location is obtained by summing the stellar UV flux $\chi_*(r) = 410\chi_0 \times (r, \text{au}/100)^{-2}$ and interstellar UV flux $\chi_{\text{IS}} = 1\text{--}100\chi_0$, which are scaled down by the visual extinction in the radial and vertical directions, respectively. We used the interstellar UV radiation field χ_0 of [Draine \(1978\)](#). Several tens of photoreaction rates are adopted from [van Dishoeck et al. \(2006\)](#)⁷. The self-shielding of H_2 from photodissociation is calculated by Eq. (37) from [Draine & Bertoldi \(1996\)](#). The shielding of CO by dust grains, H_2 , and the CO self-shielding is calculated using a precomputed table of [Lee et al. \(1996; Table 11\)](#).

The stellar X-ray radiation is modeled using Eqs. (4), (7)–(9) from [Glassgold et al. \(1997a,b\)](#), with an exponent $n = 2.81$, a cross section at 1 keV of $\sigma_{-22} = 0.85 \times 10^{-22} \text{ cm}^2$, and total X-ray luminosity of $L_{\text{XR}} = 10^{31} \text{ erg s}^{-1}$. The X-ray emitting source is assumed to be 12 stellar radii above the star. This makes X-ray ionization dominate over the cosmic ray (CR) ionization in the disk molecular layer. The standard CR ionization rate is assumed to be $\zeta_{\text{CR}} = 1.3 \times 10^{-17} \text{ s}^{-1}$. Ionization due to the decay of short-living radionuclides (SLR) is taken into account, with the SLR ionization rate of $\zeta_{\text{RN}} = 6.5 \times 10^{-19} \text{ s}^{-1}$ ([Finocchi et al. 1997](#)).

The gas–grain interactions include the sticking of neutral species and electrons to dust grains with 100% probability and desorption of ices by thermal, CRP-, and UV-driven processes. Uniform amorphous silicate particles of olivine stoichiometry were used, with a density of 3 g cm^{-3} and a radius of $0.1 \mu\text{m}$. Each grain provides 1.88×10^6 surface sites for surface recombinations ([Biham et al. 2001](#)), which proceed through the Langmuir–Hinshelwood mechanism (e.g., [Hasegawa et al. 1992](#)). The UV photodesorption yield of 10^{-5} was adopted ([Cruz-Díaz et al. 2016; Bertin et al. 2016](#)). Photodissociation processes of solid species are taken from [Garrod & Herbst \(2006\)](#) and [Semenov & Wiebe \(2011\)](#). We assumed a 1% probability for chemical desorption ([Garrod et al. 2007; Vasyunin & Herbst 2013](#)). The standard rate equation approach to the surface chemistry was utilized. Overall, the disk chemical network consists of 654 species made of 12 elements, including dust grains, and 7299 reactions.

⁷ <http://www.strw.leidenuniv.nl/~ewine/photo>

Table 4. Initial abundances used for the DM Tau chemical modeling.

Species	Relative abundances
H_2	0.499
H	2.00(−3)
He	9.75(−2)
C	7.86(−5)
N	2.47(−5)
O	1.80(−4)
S	9.14(−8)
Si	9.74(−9)
Na	2.25(−9)
Mg	1.09(−8)
Fe	2.74(−9)
P	2.16(−10)
Cl	1.00(−9)

The age of the DM Tau system is $\sim 3\text{--}7$ Myr ([Simon et al. 2000](#)); we used 5 Myr in the chemical simulations. The “low metals” elemental abundances of [Graedel et al. \(1982\)](#), [Lee et al. \(1998\)](#), and [Agúndez & Wakelam \(2013\)](#) were utilized (see Table 4). Parameters of the “standard” (or reference) DM Tau disk model are summarized in Table 5.

5. Results

Using the DM Tau disk physical and chemical model presented above, we performed about 20 detailed chemical calculations by varying various physical and chemical parameters as shown in Table 6. The results are compared to the reference model summarized in Table 5. The computed abundances of sulfur species at 5 Myr were vertically integrated to obtain radial distributions of the column densities. After that, medians of these column densities were computed at radii between 100 and 800 au and compared with the best-fit disk-averaged quantities derived with RADEX and the best-fit values at the radius of 300 au derived with DiskFit (see Figs. 7–14 and related discussion).

The key result of our study is that the observed CS column density and the sensitive upper limits for other S-bearing species can only be matched when the gas has a non-solar metallicity with a C/O ratio of ≈ 1 (see Fig. 14). Another favorable model has a solar C/O ratio of 0.46 but requires a rather low X-ray luminosity of $\lesssim 10^{29} \text{ erg s}^{-1}$, and a low initial sulfur abundance of $\lesssim 10^{-8}$ (Fig. 11). In all the other cases the observed and modeled CS/SO ratios disagree.

Another key result of our modeling is that a combination of sulfur-bearing molecules, if detected in disks, could provide very useful and unique diagnostics of a variety of disk physical and chemical processes. The summary of which sulfur-bearing species and what ratios are sensitive to what specific disk physical and chemical parameters is presented in Table 7. The CS/SO and CS/SO₂ ratios are mainly sensitive to the local gas-phase C/O elemental ratio. The presence of abundant SO and SO₂ in the gas indicates either their more efficient surface synthesis via fast diffusivity of S, O, and other heavy radicals, or more efficient release of SO, SO₂ ices into the gas phase (shocks, high-energy irradiation, turbulent transport). In ideal circumstances when H₂S, OCS, and H₂CS could also be observed in a disk, one could even determine which process is dominating.

Table 5. Parameters of the standard DM Tau disk model.

Parameter	Symbol	Value
Star		
Distance	d_*	140 pc
Temperature	T_{eff}	3720 K
Radius	R_*	$1.2 R_{\odot}$
Mass	M_*	$0.65 M_{\odot}$
UV flux at 100 au	χ_*	$410\chi_0$
X-ray luminosity ^a	L_X	$10^{31} \text{ erg s}^{-1}$
Disk		
Accretion rate	\dot{M}	$5 \times 10^{-9} M_{\odot} \text{ yr}^{-1}$
Viscosity	α	10^{-2}
Mass	M_d	$6.65 \times 10^{-2} M_{\odot}$
Surface density at 1 au	Σ_0	$4.182 \times 10^{24} \text{ cm}^{-2}$
Inner radius	r_{in}^d	0.03 au
Outer radius	r_{out}^d	800 au
Gas-to-dust mass ratio	m_{gd}	100
X-ray ionization exponent	n	2.81
X-ray cross section at 1 keV	σ_{-22}	$0.85 \times 10^{-22} \text{ cm}^2$
CRP ionization rate	ζ_{CRP}	$1.3 \times 10^{-17} \text{ s}^{-1}$
SLR ionization rate	ζ_{SLR}	$6.5 \times 10^{-19} \text{ s}^{-1}$
Chemistry		
Average grain radius	a_d	$0.1 \mu\text{m}$
Average grain density	ρ_d	3 g cm^{-3}
Sticking coefficient ^b	S	1
Amount of surface sites	N_s	1.88×10^6
UV photodesorption yield	Y_{UV}	10^{-5}
Chemical desorption yield	Y_{CD}	10^{-2}

Notes. ^(a)The X-ray emitting source assumed to be located at 12 stellar radii above the star. ^(b)We assume that H_2 does not stick to dust grains.

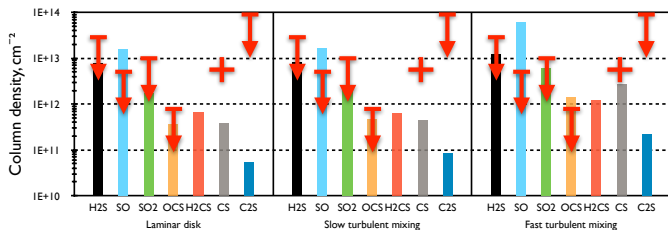


Fig. 7. The observed and computed median column densities of the key sulfur-bearing species at $r = 100\text{--}800$ au in the DM Tau disk at 5 Myr are compared. Cross indicates the CS column density and the arrows indicate the upper limits of the observed column densities for other S-bearing molecules. *Left to right panels:* three scenarios of turbulent mixing are considered: (1) laminar disk ($Sc = \infty$), (2) slow mixing ($Sc = 100$), and (3) fast mixing ($Sc = 1$; Semenov & Wiebe 2011).

5.1. Impact of turbulent mixing

The turbulent transport in disks enriches chemistry by bringing chemical ingredients from cold and dark outer regions to those where reactions with barriers, ice evaporation, and mild high-energy processing of gas and ices become active (see e.g., Illgner et al. 2004; Heinzeller et al. 2011; Semenov & Wiebe 2011; Furuya & Aikawa 2014). This is particularly true for refractory ices and/or species produced at least partly by surface reactions, including sulfurette molecules. As a result of transport, all sulfur species show a uniform increase in column densities by $\lesssim 3\text{--}10$, especially when the mixing is fast (see Fig. 7).

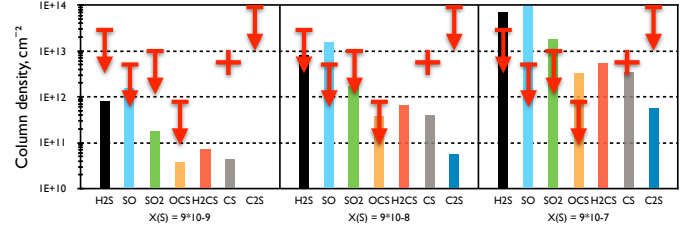


Fig. 8. As Fig. 7 but for sulfur initial elemental abundances. The cross indicates the CS column density and the arrows indicate the upper limits of the observed column densities for other S-bearing molecules. *Left to right panels:* three sets of initial elemental sulfur abundances are considered: (1) $X(\text{S}) = 9 \times 10^{-9}$, (2) $X(\text{S}) = 9 \times 10^{-8}$, and (3) $X(\text{S}) = 9 \times 10^{-7}$.

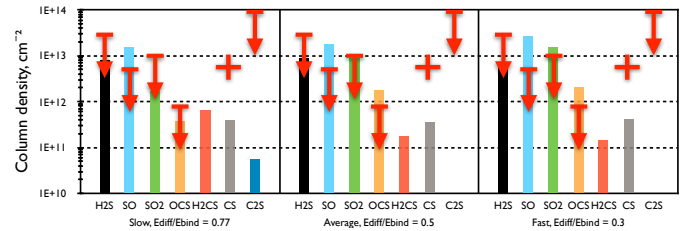


Fig. 9. As Fig. 7 but for surface diffusivities. The cross indicates the CS column density and the arrows indicate the upper limits of the observed column densities for other S-bearing molecules. *Left to right panels:* three scenarios for the surface diffusivity are considered: (1) slow diffusion, $E_{\text{diff}}/E_{\text{bind}} = 0.77$, (2) average diffusion, $E_{\text{diff}}/E_{\text{bind}} = 0.5$, and (3) fast diffusion, $E_{\text{diff}}/E_{\text{bind}} = 0.3$.

Consequently, such an uniform increase does not strongly affect the computed CS/SO ratio, which remains similar in the laminar ($\text{CS}/\text{SO} \approx 0.026$) and the fast turbulent mixing ($\text{CS}/\text{SO} \approx 0.044$) cases. Both these values are too low compared with our observations showing $\text{CS}/\text{SO} \gtrsim 1$.

5.2. Impact of initial sulfur abundances

Another crucial factor that has an impact on the outcome of sulfur chemistry is the total amount of elemental sulfur available for chemistry. The higher the initial sulfur elemental abundance that is not locked inside dust grains, the higher the computed abundances and column densities for the sulfur molecules and ices. The response of disk sulfur chemistry to the linear increase of the initial sulfur elemental abundance in our model is almost linear (see Fig. 8). This again means that the resulting CS/SO ratio remains too low, ~ 0.02 , as compared to our interferometric observations showing $\text{CS}/\text{SO} \gtrsim 1$.

5.3. Impact of surface diffusivities

Unlike the previous two parameters, the pace of surface chemistry regulated by the surface diffusivities affects the disk sulfur chemistry differently (Fig. 9). The molecules SO_2 , OCS, and to a lesser degree SO can be efficiently produced via surface processes involving S, O, CO, or SO only when these heavy ices are mobile and hence benefit from the fast, $E_{\text{diff}}/E_{\text{bind}} = 0.3$, diffusion. The H_2S that is also produced on grains does not benefit that much from faster diffusivities because it is formed via direct hydrogenation of S and H atoms can rapidly scan the dust surfaces even at $T = 10\text{--}20$ K and when the assumed diffusivity is slow, $E_{\text{diff}}/E_{\text{bind}} = 0.77$. Other S-bearing species show two distinct trends. While CS and partly SO, synthesized mainly in the

Table 6. Grid of DM Tau models computed by varying key disk physical and chemical parameters.

Parameter	Values		
	Low	Medium	High
Turbulent mixing efficiency*	$Sc = \infty$	$Sc = 100$	$Sc = 1$
Average grain size	$0.1 \mu\text{m}$	$1.0 \mu\text{m}$	$10.0 \mu\text{m}$
$E_{\text{diff}}/E_{\text{bind}}$	0.3	0.5	0.77
Initial S-abundance	9×10^{-9}	9×10^{-8}	9×10^{-7}
X-ray luminosity	$10^{29} \text{ erg s}^{-1}$	$10^{30} \text{ erg s}^{-1}$	$10^{31} \text{ erg s}^{-1}$
Interstellar UV field	$1\chi_0$	$10\chi_0$	$100\chi_0$
CRP ionization	$1.3 \times 10^{-18} \text{ s}^{-1}$	$1.3 \times 10^{-17} \text{ s}^{-1}$	$1.3 \times 10^{-16} \text{ s}^{-1}$
C/O ratio	0.46	1.0	1.2

Notes. (*)The parameters of the “standard” DM Tau disk model are marked with boldface.

Table 7. Sulfur-bearing tracers of outer disk parameters.

Physical Processes	Outer disk (>100 AU)		
	Correlate	Do not correlate	Anti-correlate
C/O ratio	CS, CCS	OCS, H ₂ CS, H ₂ S	SO, SO ₂
Surface diffusivity	SO ₂ , OCS	SO, CS, H ₂ S	CCS, H ₂ CS
Turbulent mixing	CS, SO, SO ₂ , OCS, CS, CCS	H ₂ CS, H ₂ S	...
X-ray luminosity	CCS*	SO, SO ₂ , OCS, H ₂ CS, H ₂ S	CS
UV intensity	SO, SO ₂ , H ₂ S	OCS, CS, CCS, H ₂ CS	...
Grain growth	CS, SO, SO ₂ , CCS	OCS, H ₂ CS, H ₂ S	...

Notes. (*)The CCS column density first decreases when the X-ray luminosity increases from 10^{29} to $10^{30} \text{ erg s}^{-1}$ but then it increases when the X-ray luminosity further increases to $10^{31} \text{ erg s}^{-1}$.

gas phase, are not strongly affected by the pace of surface chemistry, the column densities of C₂S and H₂CS decline when the surface diffusivities increase. For these two species the decline is caused by the competition between the two main C-reservoirs, CO and CH₄. The synthesis of CH₄ greatly benefits from faster diffusion, which lowers gas-phase abundances of other simple hydrocarbons like CH and CH₃, out of which C₂S and H₂CS are produced. As above, the modeled CS/SO ratios when the surface diffusivities are varied remain too low compared to the observations.

5.4. Impact of grain growth

The main effect of grain growth on disk chemistry, when the total dust/gas ratio does not severely change, is the reduction of the grain surface available for accretion (per unit gas volume). The disk sulfur chemistry reacts to the uniform grain growth from the ISM-like $0.1 \mu\text{m}$ -sized grains to the $10 \mu\text{m}$ -sized grains by increasing abundances and column densities of nearly all S-species due to their less severe freeze-out and more efficient gas-phase chemistry with S, particularly for SO and SO₂ (see Fig. 10). The only species that shows an opposite trend is H₂S, whose column densities decrease by a small factor of two (from $8 \times 10^{12} \text{ cm}^{-2}$ to $4 \times 10^{12} \text{ cm}^{-2}$) with grain growth. This species is produced almost entirely by the surface hydrogenation of sulfur and its production efficiency suffers from the reduced grain surface available for this process. Grain growth, as the other disk parameters discussed above, does not bring the modeled CS/SO ratios of ≈ 0.026 , ≈ 0.018 , and ≈ 0.009 (for the 0.1 , 1 , and $10 \mu\text{m}$ -sized grains, respectively) to the observed value of ≥ 1 .

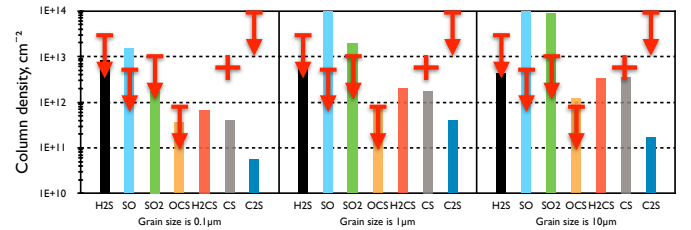


Fig. 10. As Fig. 7 but for grain sizes. The cross indicates the CS column density and the arrows indicate the upper limits of the observed column densities for other S-bearing molecules. *Left to right*: three uniform dust grain sizes are considered: (1) $0.1 \mu\text{m}$, (2) $1 \mu\text{m}$, and (3) $10 \mu\text{m}$.

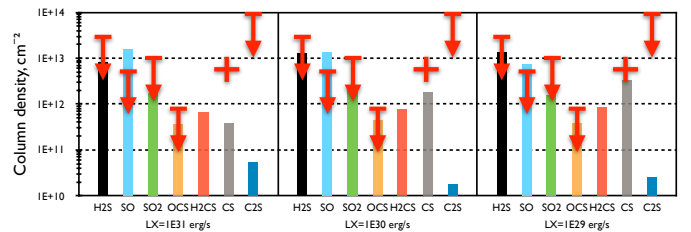


Fig. 11. As Fig. 7 but for stellar X-ray luminosities. The cross indicates the CS column density and the arrows indicate the upper limits of the observed column densities for other S-bearing molecules. *Left to right panels*: three cases of stellar X-ray luminosities are considered: (1) $L_X = 10^{31} \text{ erg s}^{-1}$, (2) $L_X = 10^{30} \text{ erg s}^{-1}$, and (3) $L_X = 10^{29} \text{ erg s}^{-1}$.

5.5. Impact of stellar X-ray luminosity

The change of the stellar X-ray luminosity affects chemistry differently for CS and SO and other sulfur species (see Fig. 11).

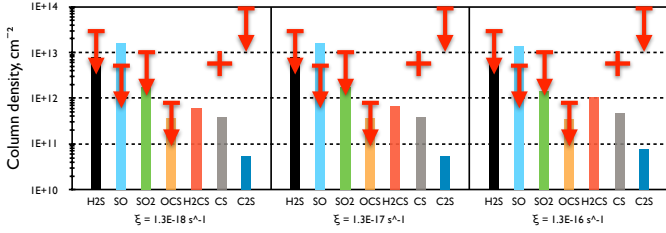


Fig. 12. As Fig. 7 but for cosmic ray ionization rates. The cross indicates the CS column density and the arrows indicate the upper limits of the observed column densities for other S-bearing molecules. *Left to right panels:* three CRP ionization rates were considered: (1) $\zeta_{\text{CRP}} = 1.3 \times 10^{-18} \text{ s}^{-1}$, (2) $\zeta_{\text{CRP}} = 1.3 \times 10^{-17} \text{ s}^{-1}$, and (3) $\zeta_{\text{CRP}} = 1.3 \times 10^{-16} \text{ s}^{-1}$.

When the adopted L_X decreases from 10^{31} to $10^{29} \text{ erg s}^{-1}$, the corresponding CS column densities increase from $\approx 4 \times 10^{11}$ to $3 \times 10^{12} \text{ cm}^{-2}$. In contrast to this, the SO column densities decrease by a factor of two from $\approx 1.5 \times 10^{13}$ to $\sim 8 \times 10^{12} \text{ cm}^{-2}$. The SO abundances decrease with decreasing X-ray ionization rate because 1) less SO molecules can be kicked out from dust grain surfaces and 2) because less oxygen can be liberated from O-bearing ices and from gaseous CO upon destruction by the X-ray-produced He^+ ions. The CS, in contrast, benefits from extra carbon liberated from CO by He^+ .

Consequently, the modeled CS/SO ratio increases from ≈ 0.026 to 0.43, getting closer to the observed value of ≥ 1 . The observed CS column density and the SO upper limits derived with DiskFit are matched with the model with the “standard” S elemental abundance of 9×10^{-8} (Table 4). In contrast, in order to better match the absolute values of the observed CS column density and the SO upper limits derived with RADEX, the model with the low stellar X-ray luminosity of $10^{29} \text{ erg s}^{-1}$ needs an additional downscaling of the initial sulfur elemental abundance by a factor of five, to the value of $\approx 2 \times 10^{-8}$.

This is the first model that fits the data and the observed CS/SO ratio, although the best-fit stellar X-ray luminosity of $10^{29} \text{ erg s}^{-1}$ seems to be too low compared to the observed X-ray properties of DM Tau. Based on the X-ray measurements with *Chandra* and *XMM* in the range of 0.3–10 keV, the quiescent stellar X-ray luminosity of DM Tau is about $10^{30} \text{ erg s}^{-1}$ (M. Guedel, priv. comm.), and can temporarily rise during the flares. This value is close to the median value representative of the X-ray luminosities measured in T Tauri stars, 10^{29} – $10^{31} \text{ erg s}^{-1}$ (e.g., Feigelson & Montmerle 1999; Telleschi et al. 2007). In the previous chemical studies of the DM Tau disk, comparable values of 2 – $100 \times 10^{29} \text{ erg s}^{-1}$ were used (Semenov & Wiebe 2011; Cleeves et al. 2014; Teague et al. 2015; Bergin et al. 2016; Rab et al. 2017b).

5.6. Impact of cosmic ray ionization

The impact of the CR ionization rate on the disk sulfur chemistry is relatively minimal (see Fig. 12). The most affected species, H_2CS , shows an increase in the column densities from 6×10^{11} to $\approx 10^{12} \text{ cm}^{-2}$ for the low and high CRP ionization rates of $1.3 \times 10^{-18} \text{ s}^{-1}$ and $1.3 \times 10^{-16} \text{ s}^{-1}$, respectively. As we mentioned in the Sect. 4.2, in our disk model the X-ray-driven ionization dominates over the CRP ionization in the disk molecular layer, where gaseous sulfur-bearing molecules have peak abundances. Thus, by varying CRP ionization rates the modeled CS/SO ratios remain too low, $\lesssim 0.035$, compared to the observed value of ≥ 1 .

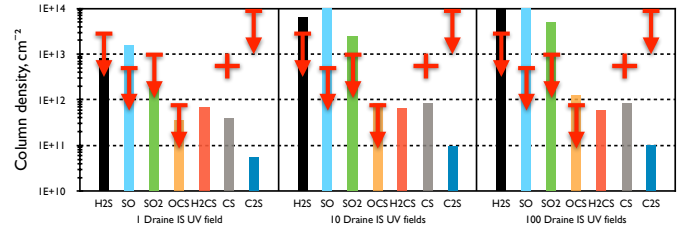


Fig. 13. As Fig. 7 but for interstellar UV radiation fields. The cross indicates the CS column density and the arrows indicate the upper limits of the observed column densities for other S-bearing molecules. *Left to right panels:* three cases of the interstellar UV radiation field are considered: (1) $1\chi_0$, (2) $10\chi_0$, and (3) $100\chi_0$, where χ_0 is the Draine (1978) IS UV field.

5.7. Impact of interstellar UV radiation

The interstellar UV radiation regulates photodissociation and photoionization of gas as well as photodesorption and photo-processing of ices. The key process for the chemistry in the disk molecular layer is photodesorption of ices. When more UV radiation penetrates into this layer, it liberates refractory ices more efficiently, increasing their gas-phase concentrations. In addition, more energetic UV-irradiation of ices creates reactive radicals including O and S, boosting the surface synthesis of chemically-related molecular ices.

This is what can be seen in Fig. 13. The heavy molecules that are mainly synthesized on grains, like SO_2 , OCS, and H_2S , show higher column densities by factors of ~ 4 – 25 for the case when the IS UV field is $\chi_{\text{UV}} = 100\chi_0$ compared to the standard $\chi_{\text{UV}} = 1\chi_0$ case. In contrast, CS, H_2CS , and CCS are produced mainly in the gas phase and hence their abundances are not that sensitive to changes of the UV radiation intensity. Consequently, by increasing the amount of the UV radiation penetrating into the DM Tau molecular layer, the resulting CS/SO ratios can only become lower, from ≈ 0.026 for the $\chi_{\text{UV}} = 1\chi_0$ model to ≈ 0.004 for the $\chi_{\text{UV}} = 100\chi_0$ model.

5.8. Impact of C/O ratios

One of the most important parameters shaping the entire disk chemistry is the total elemental C/O ratio, as well as the degree of carbon and oxygen depletion. As soon as the C/O ratio switches from < 1 to > 1 , the abundances of many oxygen-bearing species drop substantially, as the majority of elemental O becomes locked in CO. In contrast, the concentrations of carbon-bearing species increase due to the availability of elemental C that is not bound in CO. This makes the CS/SO and CS/SO₂ ratios extremely sensitive to the local disk C/O ratio (see Fig. 14).

The column densities of SO and SO₂ in our DM Tau model drop by factors of ~ 100 and 500, respectively, when the C/O ratio changes from 0.46 to 1.2. In contrast, the column densities of CS, CCS, and H_2CS are increased by factors of ~ 100 , 35, 2, respectively. The column densities of H_2S do not change as it contains neither C nor O. The column densities of OCS also do not strongly change because this molecule has an efficient surface formation route via $\text{CO} + \text{S}$, and hence follows the CO evolution.

As a result, the modeled CS/SO ratio increases from the “standard” low value of ≈ 0.026 ($\text{C/O} = 0.46$) to the values of 13 ($\text{C/O} = 1.0$) and 282 ($\text{C/O} = 1.2$). The trend continues with increasing C/O ratio: for $\text{C/O} = 2$ the modeled CS/SO ratio is 498. As can be clearly seen in Fig. 14, the modeled and observed data agree reasonably well (taking modeling uncertainties of a factor of approximately three to ten into account).

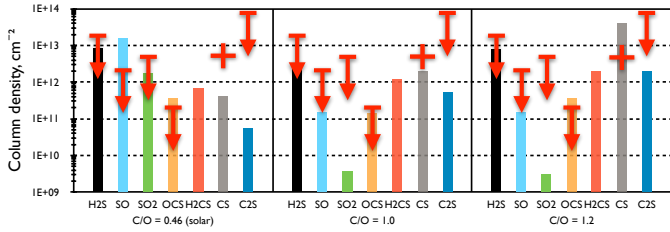


Fig. 14. As Fig. 7 but for elemental C/O ratios. The cross indicates the CS column density and the arrows indicate the upper limits of the observed column densities for other S-bearing molecules. *Left to right panels:* three elemental C/O ratios are modeled: (1) the solar C/O ratio of 0.46, (2) the C/O ratio of 1.0, and (3) the C/O ratio of 1.2.

5.9. Analysis of sulfur chemistry

We used our chemical analysis software to identify the key gas-phase and surface formation and destruction pathways for CS, SO, SO₂, OCS, and H₂S at a representative outer disk radius of 230 au of the “standard” DM Tau model with the solar C/O elemental composition, as in [Semenov & Wiebe \(2011\)](#). At this radius the temperature ranges between ≈ 9 and 50 K, the gas density is between ≈ 75 and 2.2×10^8 cm⁻³, and the visual extinction ranges between 0 and 62 magnitudes. We should note that freeze-out and desorption processes are considered in the chemical modeling, but are not listed in [Table A.1](#).

The sulfur chemistry in outer disk regions begins with S⁺ reacting with light hydrocarbons such as CH₃, CH₄, C₂H, C₃H, producing HCS⁺, HC₃S⁺, C₂S⁺, or C₃S⁺ ions, respectively. The light hydrocarbons are rapidly formed via gas-phase chemistry of C⁺ and later almost entirely converted to CO or freeze out. The sulfur-bearing ions dissociatively recombine with electrons, producing smaller neutral sulfurette molecules. Other slower initial formation routes involve barrierless neutral–neutral reactions with atomic sulfur, for example, S + CH, OH, CH₂, or C₂, forming CS or SO. At later times, the evolution of sulfur-bearing species is governed by a closed cycle where protonation processes (via HCO⁺, H₃O⁺, H₃⁺) are equilibrated by the dissociative recombination reactions, and, for some species, by gas-grain interactions and surface chemistry. In the following we describe disk chemistry for the individual sulfur-bearing molecules in detail.

The chemical evolution of CS proceeds essentially in the gas phase. The molecule CS is synthesized by dissociative recombination of C₂S⁺, C₃S⁺, HCS⁺, HC₂S⁺, and H₃CS⁺, and by slower neutral–neutral reactions S + CH, CH₂, or C₂ and, later, by the SO + C reaction. The major destruction pathways are freeze-out ($T \lesssim 30$ K), slow neutral–neutral reaction CS + CH \rightarrow C₂S + H, charge transfer with ionized hydrogen atoms, and protonation reactions (see [Table A.1](#)).

In contrast, the chemical evolution of H₂S is governed by the surface processes. The key reaction for H₂S is the surface hydrogenation of HS followed by desorption. In turn, HS ice can be produced by the hydrogenation of surface S atoms, or by the freeze-out of the gaseous HS formed via the S + OH reaction. The major destruction pathways for H₂S is freeze-out onto dust surfaces (at $T \lesssim 40$ –45 K), charge transfer reaction with atomic hydrogen, destruction via ion–molecule reaction with C⁺, and protonation reactions.

The chemical evolution of SO and SO₂ is tightly linked and occurs in the gas and ice phases. The sulfur monoxide SO is produced by the slow oxidation of S, neutral–neutral reactions between S and OH and O with HS, and surface reactions between oxygen and S or HS ices. The molecule SO is mainly destroyed

by exothermic neutral–neutral reactions with O, C, OH, freeze-out ($T \lesssim 40$ K), charge transfer reactions with atomic hydrogen, and protonation reactions.

Sulfur dioxide SO₂ is synthesized by the neutral–neutral reactions between SO and OH, slow radiative association of SO and O, and the same SO + O reaction occurring on the dust surfaces. The SO₂ major removal channels are freeze-out at $T \lesssim 60$ –80 K, ion–molecule reaction with C⁺ and neutral–neutral reaction with C, and protonation reactions.

Finally, the chemical evolution of OCS begins with the oxidation of HCS and radiative association of S and CO. The molecule OCS can also be produced by the surface recombination of S and CO as well as CS and O ices. The removal of OCS includes freeze-out ($T \lesssim 45$ K), destruction via ion–molecule reaction with C⁺, charge transfer reactions with H atoms, and protonation reactions.

6. Discussion

6.1. Comparison with previous studies of sulfur chemistry

While many sulfur-bearing species have been routinely observed in low-mass star-forming regions, the previous searches have found only very few S-bearing species in disks, mostly CS (e.g., [Dutrey et al. 2014](#)). One of the first detailed studies of the sulfur chemistry around LkCa 15, MWC 480, DM Tauri, and GO Tauri, using the IRAM 30-m antenna and the gas-grain NAUTILUS chemical code, was performed by [Dutrey et al. \(2011\)](#). No H₂S 1_{1,0} – 1_{0,1} emission at 168.8 GHz and SO 2_{2,3} – 1_{1,2} emission at 99.3 GHz were detected. The comprehensive analysis of the upper limits for SO and the detected CS emission pointed to an elemental C/O ratio of 1.2, albeit that the H₂S upper limits were not reproduced, suggesting that either H₂S remains locked onto grain surfaces or reacts with other species.

Our results agree with these finding, as our best-fit model also requires an elemental C/O ratio of ≥ 1 in the molecular layer of the DM Tau disk (see [Fig. 14](#)). In this scenario almost all of the oxygen is bound in CO and too little O is available for synthesis of other O-bearing species, including SO and SO₂. We cannot constrain the C/O ratio in the molecular layer more accurately due to the non-detection of SO and SO₂ and other S-bearing species and the poorly known abundance of elemental sulfur available for disk chemistry. Unlike in [Dutrey et al. \(2011\)](#), our sensitive upper limit of the H₂S column density is well explained by all models except the model with high elemental sulfur abundance or high UV intensity (see [Figs. 8 and 13](#)). Our modeling shows that the H₂S abundance is not sensitive to other disk physical and chemical properties (see [Table 7](#)).

Thus, the combination of CS, SO, or SO₂, and H₂S lines (or very stringent upper limits) may allow us in the future to more reliably constrain both the C/O ratio and the sulfur elemental abundance in the molecular layers of disks with well-known physical structure.

In addition, our models can explain the upper limits of the H₂S column density, where the previous study by [Dutrey et al. \(2011\)](#) failed to reproduce it. To find the reason for this discrepancy, we first compared the gas-phase and grain surface networks that were used in [Dutrey et al. \(2011\)](#) and found that they are fairly similar. Next, the gas-phase abundance and column density of H₂S in the outer part of the DM Tau disk is controlled by the freeze-out and desorption and thus is sensitive to the adopted disk temperature structure. [Dutrey et al. \(2011\)](#) used a two-layered parametric disk model and considered a representative radius of 300 au. At that radius, the midplane has a

temperature of 10 K and extends vertically up to $z/H_r \approx 1.5$. Above the midplane, a molecular layer with a temperature of ~ 17 K begins. In comparison, in our disk model at $r = 300$ au the midplane has a temperature of 12 K and extends vertically up to $z/H_r \approx 1$, after which a warmer molecular layer begins (with temperatures up to ~ 30 – 40 K). Finally, we present the median H_2S column densities over the outer 100–800 au region. In fact, in our DM Tau model the H_2S column densities increase toward the outer edge of the disk, and at $r = 300$ au the typical values of $N(\text{H}_2\text{S})$ are about 10^{13} – a few times 10^{13} cm^{-2} . These values are comparable with the values at $r = 300$ au calculated by Dutrey et al. (2011), given the modeling uncertainties of several factors.

Guilloteau et al. (2013) performed a chemical survey of 42 T Tauri and Herbig Ae systems located in the Taurus–Auriga region with the IRAM 30 m antenna (one hour/source integration), including the SO emission line. They detected SO in seven sources, which also showed strong H_2CO emission. The observed SO line profiles suggest that the emission is coming from outflows or envelopes rather than from Keplerian rotating disks. Later, Guilloteau et al. (2016) performed a deeper survey of 30 disks in Taurus–Auriga with the IRAM 30 m antenna (with about one hour/source integration), targeting two SO lines. In addition to many CS detections, they detected SO in four T Tauri and Herbig Ae sources, which traces predominantly outflow or shocked regions.

The SO molecule has also been detected and imaged in the transitional disk around the Herbig A0 star AB Aur by Pacheco-Vázquez et al. (2016). They found that the SO emission has a ring-like shape and that SO is likely depleted from the gas phase in the horseshoe-shaped dust trap in the inner disk. Recently, Booth et al. (2018) detected two SO 7 – 6 emission lines in the HD 100546 disk at around 300 GHz and found that the SO emission does not come solely from the Keplerian disk, but likely traces either a disk wind, an inner disk warp (seen in CO emission), or an accretion shock from a circumplanetary disk associated with the proposed protoplanet embedded in the disk at 50 au.

Indeed, SO and SO_2 are widely used as shock tracers in the studies of high-mass star-forming regions or low-mass Class 0 and I protostars and bipolar outflows associated with the low mass stars (Pineau des Forets et al. 1993; Tafalla et al. 2010; Esplugues et al. 2014; Gerner et al. 2014). Recently, Podio et al. (2015) observed SO emission rings around the Class 0 protostars L1527 and HH212, which likely trace shocked gas at the disk-envelope interface. As we have shown in Sect. 5.9, SO and SO_2 are partly produced via dust surface process and remain frozen at $T \lesssim 45$ – 80 K, while CS is produced in the gas phase and is more volatile, with an evaporation temperature of ~ 30 K. Thus, shocks or elevated temperatures available in the inner, $r \lesssim 30$ – 100 au regions of T Tauri disks are required to effectively put SO and SO_2 ices back into the gas phase, while in the outer disks SO and SO_2 desorption is less efficient and driven by CRP-induced or interstellar UV photons. Apparently, this is not the case for the quiescent DM Tau disk (or, at least, its outermost regions).

6.2. The non-solar C/O ratios in disks as traced by CS/SO

Our main finding is that the observed data are best explained by a C/O ratio greater than one. This agrees well with the other recent observational results. Bergin et al. (2016) have observed C_2H in both TW Hya and DM Tau with ALMA, and also found cyclic C_3H_2 in TW Hya. These hydrocarbons show bright emission rings arising at the edge of the millimeter-sized dust disk, which

can only be reproduced in the chemical models with a C/O ratio >1 and a strong UV field in molecular layers, as in our study. They explained the effect of non-solar C/O ratios in the molecular layer by predominant removal of oxygen in the form of water ice into the dark and cold midplane by the sedimentation of large, pebble-sized dust grains. This leads to a stratified C/O structure in the disk with higher ratios within the UV-dominated upper layer and solar-like C/O ratios in the ice-rich disk midplane.

A similar result was obtained by Kama et al. (2016), who have observed the CI, OI, C_2H , CO, and CII lines to constrain the carbon and oxygen abundances in TW Hya and HD 100546. To match the observations, a strong depletion of the C and O reservoirs in the cold T Tauri disk around TW Hya is required, but the warmer disk around HD 100546 is much less depleted. Both disks, however, needed a model with C/O > 1 in order to match the observations. The strong C and O depletion in TW Hya has also been confirmed by the CO isotopologue observations and detailed modeling of Schwarz et al. (2016). McClure et al. (2016) have also found a moderate C and O depletion in DM Tau and a strong depletion of the C and O reservoirs in GM Aur. The authors proposed a mechanism of locking the refractory O-rich ices (like H_2O) by the sedimentation of grains into the dark midplane where it cannot easily desorb back into the gas phase.

This mechanism of volatile depletion in disks has been investigated by Du et al. (2015) and Krijt et al. (2016). Du et al. (2015) have proposed that the elemental C and O abundances can be reduced in the upper layers of the outer disk as major C- and O-bearing volatiles reside mainly at the midplane, locked up in the icy mantles of millimeter-sized dust grains partly decoupled from the gas, which hence cannot be transported upward by turbulence. Krijt et al. (2016) have developed a dynamical model of evolving dust grains in a disk. They found that dust coagulation enhanced by the presence of ice mantles benefits dust growth and hence dust vertical settling, leading to a strong depletion of water in the disk atmosphere, where the gas-phase C/O becomes ~ 1 and higher. This removal mechanism is supported by the previous dynamical studies of evolving dust grains in disks and laboratory experiments (e.g., Birnstiel et al. 2010; Piso et al. 2015; Musiolik et al. 2016).

An alternative explanation has been proposed by Favre et al. (2013). They obtained a low disk-averaged gas-phase CO abundance in TW Hya and inferred that this could be due to chemical destruction of CO by the X-ray-produced He^+ ions, followed by rapid formation of heavy carbon chains that freeze-out onto dust grains, while oxygen goes into the synthesis of other species, like CO_2 , water, or complex organic molecules. In our disk chemical model the destruction of CO by the X-ray-produced He^+ ions occurs only in the upper layers at $r \lesssim 3$ – 10 au and hence cannot explain the derived C/O ratio of ≥ 1 from our sulfur data probing the outer, >100 au region of the DM Tau disk.

6.3. Sulfur chemistry as tracer of water snowline in disks

A defining feature for planet formation is the water snowline that shapes the properties of emerging planets (Birnstiel et al. 2016). It is temperature-, pressure-, and composition-dependent, and has a value of $T \sim 140$ – 160 K, which corresponds to the radial distances of ~ 1 – 3 au in a typical T Tauri disk (van Dishoeck et al. 2014). Condensation of water is connected to the C/O ratio of gas and ices in protoplanetary disks (Bergin et al. 2015; Öberg & Bergin 2016). Despite its importance to protoplanetary disk evolution and planet formation, a direct detection of the water snowline in protoplanetary disks is still missing.

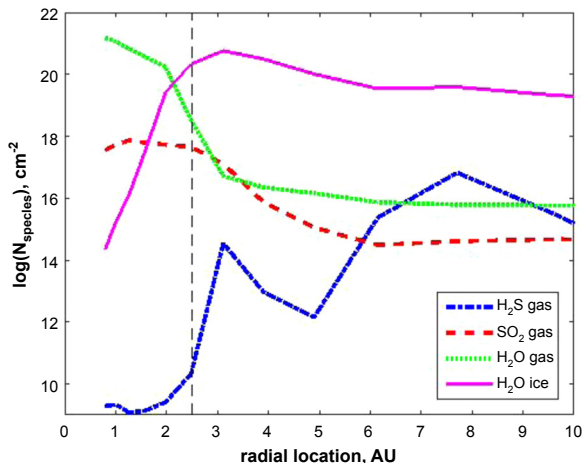


Fig. 15. Our DM Tau chemical model suggests a relationship between the column densities of H₂S, SO₂, and H₂O. The black vertical line marks the snowline location at ~ 2.5 .

While the chemical modeling of the DM Tau disk presented above was mainly focused on the interpretation of the outer-disk averaged sulfur chemistry, our model shows another interesting result, namely, a close relationship between the column densities of H₂S, SO₂, and H₂O in the inner disk region at < 10 au (Fig. 15). Specifically, a three-orders-of-magnitude rise in the column density of SO₂ is observed starting at ~ 4 – 5 au, which is at a distance about two times larger than the snowline location of ~ 2 – 2.5 au. The rise in SO₂ prior to and inside the snowline is caused by the faster surface synthesis due to increased grain temperatures and more rapid thermal hopping and desorption of water ice that brings oxygen back to the gas phase and enables faster SO₂ gas-phase chemistry. The molecule H₂S shows the opposite trend, with a rapid decrease in column density of six orders of magnitude inside the snowline. This is due to the fact that H₂S forms efficiently on dust grains, which formation is effective only at low temperatures of $\lesssim 20$ – 40 K and limited by hydrogen residence time on grains. At higher temperatures sulfur surface chemistry begins to produce heavier O-bearing sulfur species like SO₂ and OCS. Potentially, these chemical trends will be able to be observed in inner disk regions with the forthcoming JWST mission.

7. Conclusions

We have performed a new search for the sulfur-bearing molecules CS, SO, SO₂, OCS, CCS, H₂CS, and H₂S in the DM Tau disk with ALMA in Cycle 3. We have detected CS and have a tentative SO₂ detection. Failure to detect sulfur-bearing molecules in DM Tau other than CS implies either efficient freeze-out of H₂S, SO, SO₂, and OCS or that this sulfur is bound in other species, possibly refractory compounds as identified in comets. For the data analysis, we merged the new CS (3–2) ALMA Cycle 3 data with our previous PdBI data and stacked the two transitions for SO, SO₂, and OCS. We employed a one-dimensional (1D) non-LTE radiative transfer code RADEX to obtain the disk-averaged CS column densities and the upper limits for the other sulfurette molecules. Also, we used a 1+1D forward-modeling tool DiskFit to derive the corresponding radial distributions. Both these methods show that the CS column density is ~ 2 – 6×10^{12} cm⁻² (with a factor of two uncertainty).

These observed values have been compared with a suite of detailed physical–chemical models of the DM Tau disk by

varying key parameters such as the elemental sulfur abundance, grain sizes, amount of high-energy radiation, turbulent mixing, C/O ratios, and surface chemistry efficiency. We found that the observed data and, in particular, the CS/SO ratio of ≥ 1 , can only be reliably explained by a disk model with a C/O ratio of ≥ 1 , in agreement with the previous studies of the sulfur content of protoplanetary disks. This is also consistent with the recent observations of bright hydrocarbon emission rings and non-solar C/O ≥ 1 ratios found in DM Tau, TW Hya, and a few other disks. The stronger depletion of oxygen-bearing S-species compared to CS is likely linked to the proposed removal mechanism of oxygen from the disk upper layers by growing and sedimenting ice-coated grains. Furthermore, our chemical modeling demonstrated that sulfur-bearing species, if more were detected in disks, could be robust tracers of other key disk properties, such as efficiency of surface reactions, grain sizes, and amount of high-energy radiation that is able to reach the disk molecular layers. Thus more sensitive observations of sulfur-bearing molecules in the disks with well-studied structures are required with ALMA and NOEMA facilities.

Acknowledgements. This paper makes use of the following ALMA data: ADS/JAO.ALMA#2015.1.00296.S. ALMA is a partnership of ESO (representing its member states), NSF (USA), and NINS (Japan), together with NRC (Canada) and NSC and ASIAA (Taiwan) and KASI (Republic of Korea), in cooperation with the Republic of Chile. The Joint ALMA Observatory is operated by ESO, au/NRAO, and NAOJ. This work was supported by the National Programs PCMI and PNPS from INSU-CNRS. DS acknowledges support from the Heidelberg Institute of Theoretical Studies for the project “Chemical kinetics models and visualization tools: Bridging biology and astronomy”. DF and CF acknowledge support from the Italian Ministry of Education, Universities and Research, project SIR (RBSI14ZRHR). This research made use of NASA’s Astrophysics Data System. The figures in this paper were constructed with the MATPLOTLIB package (Hunter 2007) and APLPY package hosted at <http://aplpy.github.io>.

References

- Agúndez, M., & Wakelam, V. 2013, *Chem. Rev.*, **113**, 8710
 Akimkin, V., Zhukovska, S., Wiebe, D., et al. 2013, *ApJ*, **766**, 8
 Ansdell, M., Williams, J. P., van der Marel, N., et al. 2016, *ApJ*, **828**, 46
 Ansdell, M., Williams, J. P., Manara, C. F., et al. 2017, *AJ*, **153**, 240
 Bergin, E. A., Cleeves, L. I., Gorti, U., et al. 2013, *Nature*, **493**, 644
 Bergin, E., Blake, G., Ciesla, F., Hirschmann, M., & Li, J. 2015, *PNAS*, **112**, 8965
 Bergin, E. A., Du, F., Cleeves, L. I., et al. 2016, *ApJ*, **831**, 101
 Bertin, M., Romanzin, C., Doronin, M., et al. 2016, *ApJ*, **817**, L12
 Biham, O., Furman, I., Pirronello, V., & Vidali, G. 2001, *ApJ*, **553**, 595
 Birnstiel, T., Dullemond, C. P., & Brauer, F. 2010, *A&A*, **513**, A79
 Birnstiel, T., Fang, M., & Johansen, A. 2016, *Space Sci. Rev.*, **205**, 41
 Boissier, J., Bockelée-Morvan, D., Biver, N., et al. 2007, *A&A*, **475**, 1131
 Booth, A., Walsh, C., Kama, M., et al. 2018, *A&A*, **611**, A16
 Brosnan, J. T., & Brosnan, M. E. 2006, *J. Nutr.*, **136**, 1636S
 Calmonte, U., Altwegg, K., Balsiger, H., et al. 2016, *MNRAS*, **462**, S253
 Chapillon, E., Dutrey, A., Guilloteau, S., et al. 2012a, *ApJ*, **756**, 58
 Chapillon, E., Guilloteau, S., Dutrey, A., Piétu, V., & Guélin, M. 2012b, *A&A*, **537**, A60
 Charnley, S. B. 1997, *ApJ*, **481**, 396
 Chen, Y.-J., Juang, K.-J., Nuevo, M., et al. 2015, *ApJ*, **798**, 80
 Cleeves, L. I., Bergin, E. A., & Adams, F. C. 2014, *ApJ*, **794**, 123
 Cridland, A. J., Pudritz, R. E., Birnstiel, T., Cleeves, L. I., & Bergin, E. A. 2017, *MNRAS*, **469**, 3910
 Cruz-Diaz, G. A., Martín-Doménech, R., Muñoz Caro, G. M., & Chen, Y.-J. 2016, *A&A*, **592**, A68
 D’Alessio, P., Calvet, N., Hartmann, L., Lizano, S., & Cantó, J. 1999, *ApJ*, **527**, 893
 Draine, B. T. 1978, *ApJS*, **36**, 595
 Draine, B. T., & Bertoldi, F. 1996, *ApJ*, **468**, 269
 Druard, C., & Wakelam, V. 2012, *MNRAS*, **426**, 354
 Du, F., Bergin, E. A., & Hogerheijde, M. R. 2015, *ApJ*, **807**, L32
 Dutrey, A., Henning, T., Guilloteau, S., et al. 2007, *A&A*, **464**, 615
 Dutrey, A., Wakelam, V., Boehler, Y., et al. 2011, *A&A*, **535**, A104

- Dutrey, A., Semenov, D., Chapillon, E., et al. 2014, *Protostars and Planets VI* (Tucson: University of Arizona Press), 317
- Espugues, G. B., Viti, S., Goicoechea, J. R., & Cernicharo, J. 2014, *A&A*, 567, A95
- Favre, C., Cleeves, L. I., Bergin, E. A., Qi, C., & Blake, G. A. 2013, *ApJ*, 776, L38
- Fedele, D., Bruderer, S., van Dishoeck, E. F., et al. 2012, *A&A*, 544, L9
- Fedele, D., Bruderer, S., van Dishoeck, E. F., et al. 2013, *A&A*, 559, A77
- Feigelson, E. D., & Montmerle, T. 1999, *ARA&A*, 37, 363
- Finocchi, F., Gail, H.-P., & Duschl, W. J. 1997, *A&A*, 325, 1264
- Furuya, K., & Aikawa, Y. 2014, *ApJ*, 790, 97
- Garrod, R. T., & Herbst, E. 2006, *A&A*, 457, 927
- Garrod, R. T., Wakelam, V., & Herbst, E. 2007, *A&A*, 467, 1103
- Gerner, T., Beuther, H., Semenov, D., et al. 2014, *A&A*, 563, A97
- Glassgold, A. E., Najita, J., & Igea, J. 1997a, *ApJ*, 480, 344
- Glassgold, A. E., Najita, J., & Igea, J. 1997b, *ApJ*, 485, 920
- Graedel, T. E., Langer, W. D., & Frerking, M. A. 1982, *ApJS*, 48, 321
- Guilloteau, S., Dutrey, A., Wakelam, V., et al. 2012, *A&A*, 548, A70
- Guilloteau, S., Di Folco, E., Dutrey, A., et al. 2013, *A&A*, 549, A92
- Guilloteau, S., Reboussin, L., Dutrey, A., et al. 2016, *A&A*, 592, A124
- Hasegawa, T. I., Herbst, E., & Leung, C. M. 1992, *ApJS*, 82, 167
- Heinzeller, D., Nomura, H., Walsh, C., & Millar, T. J. 2011, *ApJ*, 731, 115
- Henning, T., & Semenov, D. 2013, *Chem. Rev.*, 113, 9016
- Henning, T., Semenov, D., Guilloteau, S., et al. 2010, *ApJ*, 714, 1511
- Hunter, J. D. 2007, *Comput. Sci. Eng.*, 9, 90
- Ilgner, M., Henning, T., Markwick, A. J., & Millar, T. J. 2004, *A&A*, 415, 643
- Kama, M., Bruderer, S., van Dishoeck, E. F., et al. 2016, *A&A*, 592, A83
- Kervella, P., Homan, W., Richards, A. M. S., et al. 2016, *A&A*, 596, A92
- Krijt, S., Ciesla, F. J., & Bergin, E. A. 2016, *ApJ*, 833, 285
- Lee, H.-H., Herbst, E., Pineau des Forêts, G., Roueff, E., & Le Bourlot, J. 1996, *A&A*, 311, 690
- Lee, H.-H., Roueff, E., Pineau des Forêts, G., et al. 1998, *A&A*, 334, 1047
- Le Roy, L., Altwegg, K., Balsiger, H., et al. 2015, *A&A*, 583, A1
- Loison, J.-C., Halvick, P., Bergeat, A., Hickson, K. M., & Wakelam, V. 2012, *MNRAS*, 421, 1476
- Long, F., Herczeg, G. J., Pascucci, I., et al. 2017, *ApJ*, 844, 99
- Loomis, R. A., Cleeves, L., Ilesedore, Öberg, K. I., Guzman, V. V., & Andrews, S. M. 2015, *ApJ*, 809, L25
- Matrà, L., MacGregor, M. A., Kalas, P., et al. 2017, *ApJ*, 842, 9
- McClure, M. K., Bergin, E. A., Cleeves, L. I., et al. 2016, *ApJ*, 831, 167
- McMullin, J. P., Waters, B., Schiebel, D., Young, W., & Golap, K. 2007, in *Astronomical Data Analysis Software and Systems XVI*, eds. R. A. Shaw, F. Hill, & D. J. Bell, *ASP Conf. Ser.*, 376, 127
- Mollière, P., van Boekel, R., Dullemond, C., Henning, T., & Mordasini, C. 2015, *ApJ*, 813, 47
- Mordasini, C., Alibert, Y., Benz, W., Klahr, H., & Henning, T. 2012, *A&A*, 541, A97
- Müller, H. S. P., Schlöder, F., Stutzki, J., & Winnewisser, G. 2005, *J. Mol. Struct.*, 742, 215
- Mumma, M. J., & Charnley, S. B. 2011, *ARA&A*, 49, 471
- Musioliok, G., Teiser, J., Jankowski, T., & Wurm, G. 2016, *ApJ*, 827, 63
- Öberg, K. I., & Bergin, E. A. 2016, *ApJ*, 831, L19
- Pacheco-Vázquez, S., Fuente, A., Baruteau, C., et al. 2016, *A&A*, 589, A60
- Parfenov, S. Y., Semenov, D. A., Henning, T., et al. 2017, *MNRAS*, 468, 2024
- Pascucci, I., Testi, L., Herczeg, G. J., et al. 2016, *ApJ*, 831, 125
- Piétu, V., Dutrey, A., & Guilloteau, S. 2007, *A&A*, 467, 163
- Pineau des Forêts, G., Roueff, E., Schilke, P., & Flower, D. R. 1993, *MNRAS*, 262, 915
- Piso, A.-M. A., Öberg, K. I., Birnstiel, T., & Murray-Clay, R. A. 2015, *ApJ*, 815, 109
- Podio, L., Codella, C., Gueth, F., et al. 2015, *A&A*, 581, A85
- Qi, C., Öberg, K. I., Wilner, D. J., et al. 2013, *Science*, 341, 630
- Rab, C., Elbakyan, V., Vorobyov, E., et al. 2017a, *A&A*, 604, A15
- Rab, C., Güdel, M., Padovani, M., et al. 2017b, *A&A*, 603, A96
- Sakai, N., Oya, Y., López-Sepulcre, A., et al. 2016, *ApJ*, 820, L34
- Schöier, F. L., van der Tak, F. F. S., van Dishoeck, E. F., & Black, J. H. 2005, *A&A*, 432, 369
- Schräpler, R., & Henning, T. 2004, *ApJ*, 614, 960
- Schwarz, K. R., Bergin, E. A., Cleeves, L. I., et al. 2016, *ApJ*, 823, 91
- Semenov, D., & Wiebe, D. 2011, *ApJS*, 196, 25
- Semenov, D., Hersant, F., Wakelam, V., et al. 2010, *A&A*, 522, A42
- Shakura, N. I., & Sunyaev, R. A. 1973, *A&A*, 24, 337
- Simon, M., Dutrey, A., & Guilloteau, S. 2000, *ApJ*, 545, 1034
- Simon, M., Guilloteau, S., Di Folco, E., et al. 2017, *ApJ*, 844, 158
- Stäuber, P., Doty, S. D., van Dishoeck, E. F., & Benz, A. O. 2005, *A&A*, 440, 949
- Suzuki, H., Yamamoto, S., Ohishi, M., et al. 1992, *ApJ*, 392, 551
- Tafalla, M., Santiago-García, J., Hacar, A., & Bachiller, R. 2010, *A&A*, 522, A91
- Teague, R., Semenov, D., Guilloteau, S., et al. 2015, *A&A*, 574, A137
- Teague, R., Guilloteau, S., Semenov, D., et al. 2016, *A&A*, 592, A49
- Teague, R., Semenov, D., Gorti, U., et al. 2017, *ApJ*, 835, 228
- Telleschi, A., Güdel, M., Briggs, K. R., Audard, M., & Palla, F. 2007, *A&A*, 468, 425
- Trapman, L., Miotello, A., Kama, M., van Dishoeck, E. F., & Bruderer, S. 2017, *A&A*, 605, A69
- van der Tak, F. F. S., Black, J. H., Schöier, F. L., Jansen, D. J., & van Dishoeck, E. F. 2007, *A&A*, 468, 627
- van Dishoeck, E. F., Jonkheid, B., & van Hemert M. C. 2006, in *Photoprocesses in Protoplanetary Disks*, eds. I. R. Sims, & D. A. Williams (Cambridge, UK: Royal Society of Chemistry), *Faraday discussion*, 133, 231
- van Dishoeck, E. F., Bergin, E. A., Lis, D. C., & Lunine, J. I. 2014, *Protostars and Planets VI* (Tucson: University of Arizona Press), 835
- Vasyunin, A. I., & Herbst, E. 2013, *ApJ*, 769, 34
- Vidal, T. H. G., Loison, J.-C., Jaziri, A. Y., et al. 2017, *MNRAS*, 435
- Wakelam, V., Herbst, E., Loison, J.-C., et al. 2012, *ApJS*, 199, 21
- Walsh, C., Loomis, R. A., Öberg, K. I., et al. 2016, *ApJ*, 823, L10
- Williams, J. P., & Best, W. M. J. 2014, *ApJ*, 788, 59
- Woitke, P., Kamp, I., & Thi, W. 2009, *A&A*, 501, 383
- Yen, H.-W., Liu, H. B., Gu, P.-G., et al. 2016, *ApJ*, 820, L25

Appendix A: Additional table

Table A.1. Key chemical processes for S-bearing species.

Reaction	α (cm^3) s^{-1}	β –	γ (K)
Ion–molecule reactions			
$\text{CH}_3 + \text{S}^+ \rightarrow \text{HCS}^+ + \text{H}_2$	5.00 (–10)	0	0
$\text{CH}_3^+ + \text{S} \rightarrow \text{HCS}^+ + \text{H}_2$	0.14 (–8)	0	0
$\text{S}^+ + \text{C}_2\text{H} \rightarrow \text{C}_2\text{S}^+ + \text{H}$	0.20 (–8)	–0.50	0
$\text{S}^+ + \text{C}_3\text{H} \rightarrow \text{C}_3\text{S}^+ + \text{H}$	0.69 (–8)	–0.50	0
$\text{S}^+ + \text{CH}_4 \rightarrow \text{H}_3\text{CS}^+ + \text{H}$	0.14 (–9)	0	0
$\text{CS}^+ + \text{H}_2 \rightarrow \text{HCS}^+ + \text{H}$	0.48 (–9)	0	0
$\text{H}^+ + \text{C}_2\text{S} \rightarrow \text{C}_2\text{S}^+ + \text{H}$	0.11 (–7)	–0.50	0
$\text{H}^+ + \text{C}_3\text{S} \rightarrow \text{C}_3\text{S}^+ + \text{H}$	0.15 (–7)	–0.50	0
$\text{CS} + \text{H}^+ \rightarrow \text{CS}^+ + \text{H}$	0.18 (–7)	–0.50	0
$\text{H}_2\text{S} + \text{H}^+ \rightarrow \text{H}_2\text{S}^+ + \text{H}$	0.38 (–8)	–0.50	0
$\text{OCS} + \text{H}^+ \rightarrow \text{HS}^+ + \text{CO}$	0.65 (–8)	–0.50	0
$\text{SO} + \text{H}^+ \rightarrow \text{SO}^+ + \text{H}$	0.14 (–7)	–0.50	0
$\text{CS} + \text{H}_3^+ \rightarrow \text{HCS}^+ + \text{H}_2$	0.11 (–7)	–0.50	0
$\text{H}_3^+ + \text{H}_2\text{CS} \rightarrow \text{H}_3\text{CS}^+ + \text{H}_2$	0.38 (–8)	–0.50	0
$\text{H}_2\text{S} + \text{H}_3^+ \rightarrow \text{H}_3\text{S}^+ + \text{H}_2$	0.23 (–8)	–0.50	0
$\text{OCS} + \text{H}_3^+ \rightarrow \text{HOCS}^+ + \text{H}_2$	0.38 (–8)	–0.50	0
$\text{SO} + \text{H}_3^+ \rightarrow \text{HSO}^+ + \text{H}_2$	0.84 (–8)	–0.50	0
$\text{SO}_2 + \text{H}_3^+ \rightarrow \text{HSO}_2^+ + \text{H}_2$	0.37 (–8)	–0.50	0
$\text{CS} + \text{H}_3\text{O}^+ \rightarrow \text{HCS}^+ + \text{H}_2\text{O}$	0.50 (–8)	–0.50	0
$\text{H}_2\text{S} + \text{H}_3\text{O}^+ \rightarrow \text{H}_3\text{S}^+ + \text{H}_2\text{O}$	0.11 (–8)	–0.50	0
$\text{CS} + \text{HCO}^+ \rightarrow \text{HCS}^+ + \text{CO}$	0.43 (–8)	–0.50	0
$\text{HCO}^+ + \text{H}_2\text{CS} \rightarrow \text{H}_3\text{CS}^+ + \text{CO}$	0.15 (–8)	–0.50	0
$\text{H}_2\text{S} + \text{HCO}^+ \rightarrow \text{H}_3\text{S}^+ + \text{CO}$	0.95 (–9)	–0.50	0
$\text{OCS} + \text{HCO}^+ \rightarrow \text{HOCS}^+ + \text{CO}$	0.15 (–8)	–0.50	0
$\text{SO} + \text{HCO}^+ \rightarrow \text{HSO}^+ + \text{CO}$	0.33 (–8)	–0.50	0
$\text{HCS}^+ + \text{O} \rightarrow \text{OCS}^+ + \text{H}$	0.50 (–9)	0	0
$\text{HCS}^+ + \text{O} \rightarrow \text{HCO}^+ + \text{S}$	0.50 (–9)	0	0
$\text{H}_2\text{S} + \text{S}^+ \rightarrow \text{S}_2^+ + \text{H}_2$	0.64 (–9)	–0.50	0
$\text{OCS} + \text{S}^+ \rightarrow \text{S}_2^+ + \text{CO}$	0.91 (–9)	–0.50	0
$\text{C}^+ + \text{C}_2\text{S} \rightarrow \text{C}_2\text{S}^+ + \text{C}$	0.17 (–8)	–0.50	0
$\text{C}^+ + \text{C}_3\text{S} \rightarrow \text{C}_3\text{S}^+ + \text{C}$	0.24 (–8)	–0.50	0
$\text{C}^+ + \text{H}_2\text{CS} \rightarrow \text{CS} + \text{CH}_2^+$	0.21 (–8)	–0.50	0
$\text{H}_2\text{S} + \text{C}^+ \rightarrow \text{HCS}^+ + \text{H}$	0.95 (–9)	–0.50	0
$\text{OCS} + \text{C}^+ \rightarrow \text{CS}^+ + \text{CO}$	0.16 (–8)	–0.50	0
$\text{OCS} + \text{C}^+ \rightarrow \text{OCS}^+ + \text{C}$	0.40 (–9)	–0.50	0
$\text{SO}_2 + \text{C}^+ \rightarrow \text{SO}^+ + \text{CO}$	0.20 (–8)	–0.50	0
Dissociative recombination reactions			
$\text{C}_2\text{S}^+ + \text{e}^- \rightarrow \text{CS} + \text{C}$	0.15 (–6)	–0.50	0
$\text{C}_2\text{S}^+ + \text{e}^- \rightarrow \text{C}_2 + \text{S}$	0.15 (–6)	–0.50	0
$\text{C}_3\text{S}^+ + \text{e}^- \rightarrow \text{C}_2\text{S} + \text{C}$	1.00 (–7)	–0.50	0
$\text{C}_3\text{S}^+ + \text{e}^- \rightarrow \text{C}_3 + \text{S}$	1.00 (–7)	–0.50	0
$\text{C}_3\text{S}^+ + \text{e}^- \rightarrow \text{CS} + \text{C}_2$	1.00 (–7)	–0.50	0
$\text{H}_3\text{CS}^+ + \text{e}^- \rightarrow \text{H}_2\text{CS} + \text{H}$	0.30 (–6)	–0.50	0
$\text{H}_3\text{S}^+ + \text{e}^- \rightarrow \text{H}_2\text{S} + \text{H}$	0.30 (–6)	–0.50	0
$\text{HC}_2\text{S}^+ + \text{e}^- \rightarrow \text{CS} + \text{CH}$	0.15 (–6)	–0.50	0
$\text{HCS}^+ + \text{e}^- \rightarrow \text{CS} + \text{H}$	0.18 (–6)	–0.57	0
$\text{HCS}^+ + \text{e}^- \rightarrow \text{CH} + \text{S}$	0.79 (–6)	–0.57	0
$\text{HOCS}^+ + \text{e}^- \rightarrow \text{CS} + \text{OH}$	0.20 (–6)	–0.50	0
$\text{HOCS}^+ + \text{e}^- \rightarrow \text{OCS} + \text{H}$	0.20 (–6)	–0.50	0
$\text{HSO}^+ + \text{e}^- \rightarrow \text{SO} + \text{H}$	0.20 (–6)	–0.50	0
$\text{HSO}_2^+ + \text{e}^- \rightarrow \text{SO}_2 + \text{H}$	0.20 (–6)	–0.50	0
$\text{HSO}_2^+ + \text{e}^- \rightarrow \text{SO} + \text{OH}$	1.00 (–7)	–0.50	0
$\text{OCS}^+ + \text{e}^- \rightarrow \text{CO} + \text{S}$	0.29 (–6)	–0.62	0
$\text{OCS}^+ + \text{e}^- \rightarrow \text{CS} + \text{O}$	0.48 (–7)	–0.62	0
$\text{OCS}^+ + \text{e}^- \rightarrow \text{SO} + \text{C}$	0.10 (–7)	–0.62	0
$\text{H}_2\text{CS}^+ + \text{e}^- \rightarrow \text{CS} + \text{H} + \text{H}$	0.30 (–6)	–0.50	0
$\text{H}_3\text{CS}^+ + \text{e}^- \rightarrow \text{CS} + \text{H} + \text{H}_2$	0.30 (–6)	–0.50	0

Table A.1. continued.

Reaction	α (cm^3) s^{-1}	β –	γ (K)
Neutral–neutral reactions without barriers			
$\text{SO} + \text{C} \rightarrow \text{CS} + \text{O}$	0.35 (–10)	0	0
$\text{SO} + \text{C} \rightarrow \text{CO} + \text{S}$	0.35 (–10)	0	0
$\text{SO}_2 + \text{C} \rightarrow \text{CO} + \text{SO}$	0.70 (–10)	0	0
$\text{CS} + \text{CH} \rightarrow \text{C}_2\text{S} + \text{H}$	1.00 (–10)	0	0
$\text{O} + \text{HCS} \rightarrow \text{OCS} + \text{H}$	0.50 (–10)	0	0
$\text{O} + \text{HS} \rightarrow \text{SO} + \text{H}$	0.16 (–9)	0.50	0
$\text{OH} + \text{SO} \rightarrow \text{SO}_2 + \text{H}$	0.86 (–10)	0	0
$\text{S} + \text{C}_2 \rightarrow \text{CS} + \text{C}$	1.00 (–10)	0	0
$\text{S} + \text{CH} \rightarrow \text{CS} + \text{H}$	0.50 (–10)	0	0
$\text{S} + \text{CH}_2 \rightarrow \text{CS} + \text{H}_2$	1.00 (–10)	0	0
$\text{S} + \text{O}_2 \rightarrow \text{SO} + \text{O}$	0.23 (–11)	0	0
$\text{S} + \text{OH} \rightarrow \text{SO} + \text{H}$	0.66 (–10)	0	0
Surface photoprocessing (CRP-induced UV photons)			
$\text{H}_2\text{S (ice)} + h\nu_{\text{CRP}} \rightarrow \text{H}_2 \text{ (ice)} + \text{S (ice)}$	5.15 (3)	0	0
$\text{H}_2\text{S (ice)} + h\nu_{\text{CRP}} \rightarrow \text{HS (ice)} + \text{H (ice)}$	8.50 (2)	0	0
$\text{OCS (ice)} + h\nu_{\text{CRP}} \rightarrow \text{CO (ice)} + \text{S (ice)}$	5.35 (3)	0	0
$\text{SO (ice)} + h\nu_{\text{CRP}} \rightarrow \text{S (ice)} + \text{O (ice)}$	5.00 (2)	0	0
$\text{SO}_2 \text{ (ice)} + h\nu_{\text{CRP}} \rightarrow \text{SO (ice)} + \text{O (ice)}$	1.88 (3)	0	0
Surface recombination reactions			
$\text{H (ice)} + \text{S (ice)} \rightarrow \text{HS (ice)}$	1.00	0	0
$\text{H (ice)} + \text{HS (ice)} \rightarrow \text{H}_2\text{S (ice)}$	1.00	0	0
$\text{O (ice)} + \text{CS (ice)} \rightarrow \text{OCS (ice)}$	1.00	0	0
$\text{O (ice)} + \text{S (ice)} \rightarrow \text{SO (ice)}$	1.00	0	0
$\text{SO (ice)} + \text{O (ice)} \rightarrow \text{SO}_2 \text{ (ice)}$	1.00	0	0
$\text{SO (ice)} + \text{C (ice)} \rightarrow \text{CO (ice)} + \text{S (ice)}$	1.00	0	0
$\text{S (ice)} + \text{CO (ice)} \rightarrow \text{OCS (ice)}$	1.00	0	0
$\text{OCS (ice)} + \text{H (ice)} \rightarrow \text{CO (ice)} + \text{HS (ice)}$	1.00	0	0
$\text{SO}_2 \text{ (ice)} + \text{H (ice)} \rightarrow \text{O}_2 \text{ (ice)} + \text{HS (ice)}$	1.00	0	0
$\text{O (ice)} + \text{HS (ice)} \rightarrow \text{SO (ice)} + \text{H (ice)}$	1.00	0	0